Mechanisms of Ageostrophic Wind Convergence in the Boundary Layer of Coastal Warm-Sector Extreme Heavy Rainfall

Fan Xia[1], Xiaogang Huang[1], Jianfang Fei[1], Ju Wang[2], XiaoPing Cheng[1], and Chi Zhang[3]

[1]College of Meteorology and Oceanography, National University of Defense Technology
[2]National University of Defense Technology
[3]Unit 94116 of PLA

January 17, 2023

Abstract

The South China coast has a high incidence of warm-sector heavy rainfall (WSHR) events. The ageostrophic winds in the boundary layer in most of these events associated with the southwesterly boundary layer jets (BLJs) mainly exhibit strong convergence at rainfall area. In this paper, we analyze two cases of WSHR in May 2013 and May 2015, which occurred in similar synoptic environments but varied in intensity, extent, and duration of rainfall, where the ageostrophic winds are the confrontational confluence and asymptotic confluence pattern, respectively. ERA-5 reanalysis data and the diagnostic equation of ageostrophic wind are used to examine the factors affecting the ageostrophic winds in the northern land region and the southern offshore region of the rainfall. The results suggest that land-sea contrast leads to the convergence of ageostrophic winds in the rainfall area. Boundary layer friction dominates the northeasterly ageostrophic winds on land. The diurnal variation of BLJs dominates the ageostrophic winds and their diurnal variation at sea, contributing southwesterly or southeasterly ageostrophic winds, so the phase difference between the land and sea forms confrontational or asymptotic confluence, respectively. BLJs with different intensities, extents, and diurnal variations can lead to different ageostrophic wind patterns and their confluence modes. The land-sea thermal contrast can directly affect ageostrophic winds, and it can also affect the diurnal variation of BLJs, thus affecting the ageostrophic winds and their confluence mode. It is further verified that the BLJs and thermal forcing are important in warm-sector heavy rainfall processes in South China.

Hosted file

953227_0_art_file_10577859_rns1sz.docx available at https://authorea.com/users/573559/articles/617795-mechanisms-of-ageostrophic-wind-convergence-in-the-boundary-layer-of-coastal-warm-sector-extreme-heavy-rainfall

Mechanisms of Ageostrophic Wind Convergence in the Boundary Layer of Coastal Warm-Sector Extreme Heavy Rainfall

Fan Xia[1], Xiaogang Huang[1,2], Jianfang Fei[1], Ju Wang[1], Xiaoping Cheng[1], and Chi Zhang[3]

[1]College of Meteorology and Oceanography, National University of Defense Technology, Changsha, China.

[2]Collaborative Innovation Center on Forecast and Evaluation of Meteorological Disasters (CIC-FEMD), Nanjing University of Information Science &Technology, Nanjing, China.

[3]Unit 94116 of PLA, Hetian, China.

Corresponding author: Xiaogang Huang (huang.x.g@163.com)

Key Points:

- Land-sea contrast leads to the strong convergence in the coastal warm-sector extreme heavy rainfall area in South China
- Marine boundary layer jets and their diurnal variation can influence the ageostrophic winds and then affect the convergence
- The land-sea thermal contrast can affect the ageostrophic winds and the convergence by changing the diurnal variation of boundary layer jets.

Abstract

The South China coast has a high incidence of warm-sector heavy rainfall (WSHR) events. The ageostrophic winds in the boundary layer in most of these events associated with the southwesterly boundary layer jets (BLJs) mainly exhibit strong convergence at rainfall area. In this paper, we analyze two cases of WSHR in May 2013 and May 2015, which occurred in similar synoptic environments but varied in intensity, extent, and duration of rainfall, where the ageostrophic winds are the confrontational confluence and asymptotic confluence pattern, respectively. ERA-5 reanalysis data and the diagnostic equation of ageostrophic wind are used to examine the factors affecting the ageostrophic winds in the northern land region and the southern offshore region of the rainfall. The results suggest that land-sea contrast leads to the convergence of ageostrophic winds in the rainfall area. Boundary layer friction dominates the northeasterly ageostrophic winds on land. The diurnal variation of BLJs dominates the ageostrophic winds and their diurnal variation at sea, contributing southwesterly or southeasterly ageostrophic winds, so the phase difference between the land and sea forms confrontational or asymptotic confluence, respectively. BLJs with different intensities, extents, and diurnal variations can lead to different ageostrophic wind patterns and their confluence modes. The land-sea thermal contrast can directly affect ageostrophic winds, and it can also affect the diurnal variation of BLJs, thus affecting the ageostrophic winds and their confluence mode. It is further verified that the BLJs and thermal forcing are important in warm-sector heavy rainfall processes in South China.

Plain Language Summary

Extremely heavy rainfall frequently occurs in coastal Southern China, which causes great damage and is difficult to accurately forecast. Most of this kind of rainfall is associated with southwesterly wind in the lower atmosphere and strong convergence of the lower airflow. Our purpose is to better understand the factors that lead to strong convergence, which is an important factor for heavy rainfall. Since the geostrophic wind component has no divergence, the convergence is mostly contributed by the ageostrophic wind component, which doesn't conform to the geostrophic balance. We find that different intensities, ranges, and diurnal changes of the southwesterly wind in the lower atmosphere can lead to different distributions of ageostrophic winds in the South China Sea. The thermal difference between land and sea can influence the diurnal change of the southwesterly wind in the lower atmosphere, and it can also affect the

ageostrophic winds and their convergence. The results will potentially provide a better understanding of heavy rainfall events in Southern China and may lead to better forecasts and issuing of warnings.

1 Introduction

South China is one of the heavy rainfall centers in China that experiences abundant rainfall in the pre-rainy season from April to June, with the rainfall accounting for 40%–60% of the annual total (Chen et al., 2014; Luo et al., 2017; Sun et al., 2019). It is a region prone to a high frequency of meteorological disasters (Wu et al., 2019). Heavy rainfall in South China can be divided into warm-sector heavy rainfall (WSHR) and frontal heavy rainfall as a result of synoptic-scale forcing (Huang, 1986; Ding, 1994). Frontal heavy rainfall usually occurs in the inland area of the northern Guangdong province and is associated with cold fronts. WSHR occurs in the warm sector that is more than 200 km ahead of the surface front or in the area where the rainfall is influenced by southerly flow in the middle and lower troposphere (Liu et al., 2019). Compared with frontal heavy rainfall, WSHR is characterized by higher intensity, higher spatial concentration, abruptness, and lower predictability (Luo et al., 2017; Huang & Luo, 2017; Du & Chen, 2018; Wu et al., 2020a, b). The coastal area of Guangdong is the main region where WSHR occurs (Sun et al., 2019). A better understanding of the mechanisms of coastal WSHR has important implications for improving prediction and warning.

The triggering mechanisms of WSHR in the South China coastal area are complex and influenced by land–sea contrast, complex coastal topography, mesoscale convergence lines, southerly low-level jets (LLJs), and other boundary layer disturbances (Huang, 1986; Lin et al., 2006; Chen et al., 2014; Du & Chen, 2018), among which LLJs have received particular attention. There is a close relationship between the low-level southwesterly jet and heavy precipitation over East Asia (Chen et al., 2005; Chen & Yu, 1988). LLJs can transport warm and humid air to South China (Huang & Luo, 2017). They can also produce strong shear instability, and the terminus of the LLJ is often associated with low-level convergence. In addition, the combination of the LLJ and topography enhances coastal convergence (Chen et al., 2017; Du & Chen, 2018, 2019a). The secondary circulation formed by LLJs can provide lifting conditions. Therefore, LLJs can provide both dynamical and thermal conditions for heavy rainfall. 76% of

WSHR events in South China are associated with LLJs (Li et al., 2021). The inland frontal rainband in southern China is closely related to the synoptic-system-related LLJ which has its peak speed between 850 and 700 hPa, while the coastal WSHR is associated with the boundary layer jets (BLJs) at 925 hPa (Du & Chen, 2019), so the behaviors of coastal WSHR are closely related to the BLJs.

The BLJs have an obvious diurnal variation with a maximum at night. Mechanisms believed to explain the diurnal variation of BLJs are mainly the Blackadar mechanism (Blackadar, 1957; Du & Rotunno, 2014) and the Holton mechanism (Holton, 1967). The Blackadar mechanism mainly considers the effect of an inertial oscillation due to the diurnal variation of boundary layer friction. The ageostrophic wind vector would rotate clockwise with time at a period of $2\pi/f$ where f is the Coriolis parameter in idealized conditions (Blackadar, 1957). If the directions of the ageostrophic wind and the geostrophic wind are the same at night, a super-geostrophic wind will appear, causing the acceleration of BLJs. The Holton mechanism mainly considers the diurnal change in the pressure gradient force due to the diurnal topographic thermal forcing. The Blackadar theory can explain the behaviors of the BLJs over the Great Plains of the United States better than the Holton mechanism (Shapiro et al., 2016). Chen et al. (2009) found the low-level winds over southern China were strongest at late night or in the early morning, and they pointed out that this diurnal change was closely related to ageostrophic wind component and suggested the clockwise rotation of wind vector at night was probably due to the inertial oscillation. Many studies show that the formation of the BLJs in China may be attributed to the combination of the two mechanisms (Chen & Yu, 1988; Du et al., 2015; Xue et al., 2018; Fu et al., 2019). To investigate the effects of the two mechanisms, Du and Rotunno (2014) proposed a simple 1D model with diurnal thermal forcing and diurnally varying boundary layer friction. This model can not only combine but also separate Blackadar and Holton mechanisms. The 1D model can roughly reproduce these mesoscale model-simulated diurnal boundary layer winds in the coastal ocean of South China (Du et al., 2015).

In addition to the diurnal variation of BLJs, studies have shown that from May to June, the diurnal thermally forced land-sea breeze circulations also affect the diurnal variation of rainfall in the Pearl River Delta (PRD) region (Chen et al., 2015). Chen et al. (2015, 2019) found that rainfall events without LLJ are more frequent than those with LLJ, and the land-sea breeze circulation is more important to the generation and propagation of convection than convergence due to the contrast of sea-land friction.

Heavy rainfall can be divided into short-duration heavy rainfall and persistent heavy rainfall according to its duration. Compared to short-duration heavy rainfall, persistent heavy rainfall processes cause more serious casualties and economic losses. Zhang et al. (2021) proposed the concept of extreme persistent heavy rainfall (EPHR). In their definition of EPHR, the duration of hourly precipitation exceeding 20 mm at a fixed location should be at least 5 hr (although there can be an interruption of up to 1 hr). Most of the coastal EPHR in South China can be classified as WSHR, and the majority of the cases are accompanied by southwest BLJs (Huang et al., 2022). In addition, in most cases, there is strong convergence in the lower troposphere in the coastal rainfall area, and the ageostrophic winds exhibit obvious confluence patterns (Huang et al., 2022). The intensity and duration of heavy rainfall events vary with different confluence patterns of the ageostrophic wind. Holton (2004) pointed out that the ageostrophic wind was influenced by the local tendency of the geostrophic wind and geostrophic advection. Yet, his conclusion was derived under the hypothesis that there was no friction in the free troposphere and the ageostrophic winds were much smaller than the geostrophic winds, which is not applicable in the lower troposphere.

Considering the role of ageostrophic wind in the diurnal change of BLJs, and the boundary layer convergence of the ageostrophic wind in the coastal WSHR in South China, we focus on the mechanisms of ageostrophic wind in our study. We attempt to investigate whether the ageostrophic winds are related to the southwest BLJs and the thermal forcing in South China, which will deepen our understanding of WSHR. We selected two typical WSHR events with different confluence patterns of the ageostrophic wind for analysis. And we have conducted a diagnostic analysis of the formation of ageostrophic winds to explore the influencing factors of the ageostrophic winds. The remainder of the paper is organized as follows. Section 2 presents the data and methods used in this study. Two cases of WSHR in South China are outlined in Section 3. Section 4 discusses the ageostrophic wind patterns and the diagnostic results, and Section 5 further elucidates the formation mechanisms of ageostrophic winds and the resulting convergence. The final section summarizes the study's results.

2 Data and Methods

2.1 Data

The hourly gauge-satellite merged precipitation product from the China Meteorological Data Service Centre (CMDC) with a spatial grid spacing of 0.1° × 0.1° is used for quantitative precipitation analysis (Shen et al., 2014). This product combines the quality-controlled hourly precipitation data from the national automatic observation stations and the Climate Prediction Center Morphing (CMORPH) satellite precipitation estimates. It has been demonstrated to accurately reflect heavy rainfall characteristics (Zhou et al., 2015).

The fifth generation of the European Centre for Medium-Range Weather Forecasts (ECMWF) atmospheric reanalysis (ERA5) hourly data on pressure levels with a horizontal grid spacing of 0.25° × 0.25° is used for the analysis of synoptic environments and wind diagnosis. ERA5 hourly data on single levels are used to analyze the convective available potential energy (CAPE) and 2-m temperature.

2.2 Barnes Filtering

To separate the ageostrophic component from the total wind, the geopotential height field should first be smoothed by the Barnes low-pass filter, also known as the Gaussian-weighted objective analysis method (Barnes, 1964; Koch et al., 1983; Barnes & Colman, 1993, 1994). This method can effectively filter small-scale noise and retain synoptic-scale or sub-synoptic-scale flow patterns. It has been widely used to separate the flow field into synoptic-, meso-, and convective scales (Xu et al., 2017; Wei et al., 2022) and study the physical mechanisms of diurnal variability of low-level ageostrophic winds (Xue et al., 2018). By using the same weight constant settings ($g = 0.3$ and $c = 30{,}000$) as Huang et al. (2022), the geopotential height is filtered to damp most of the waves shorter than 500 km and obtain most of the geostrophic motion with wavelengths greater than 1000 km, so the ageostrophic scales are mostly damped. Then the geostrophic wind component is computed from the filtered geopotential height fields. The ageostrophic wind is obtained by subtracting the geostrophic wind from the total wind.

2.3 Diagnostic Equation of Ageostrophic Winds

Since the geostrophic and quasi-geostrophic approximation conditions are not satisfied during the WSHR events in South China and the turbulent friction effects should be considered in the boundary layer, we need to derive the diagnostic equation of ageostrophic wind from the original horizontal momentum equation in the pressure (P) coordinate system:

$$\frac{d\vec{V}}{dt} = -\nabla_p \Phi - f\vec{k} \times \vec{V} + \vec{F_h} \ , \tag{1}$$

where $\vec{V}$ is the total wind, Φ is the geopotential height, f is the Coriolis parameter, $\vec{F_h}$ is the friction force, and $\vec{k}$ is the unit vector in the vertical direction. Decomposing the total wind into geostrophic and ageostrophic winds on the right-hand side: $\vec{V} = \vec{V_g} + \vec{V_a}$, neglecting the variation of f with latitude and adhering to the definition of the geostrophic wind $\vec{V_g} = -\frac{1}{f}\nabla_p \Phi \times \vec{k}$, we get

$$\vec{V_a} = \frac{1}{f}\vec{k} \times \frac{d\vec{V}}{dt} - \frac{1}{f}\vec{k} \times \vec{F_h} \ , \tag{2}$$

then expanding the total derivative, we get

$$\vec{V_a} = \frac{1}{f}\vec{k} \times \frac{\partial \vec{V}}{\partial t} + \frac{1}{f}\vec{k} \times \left[\left(\vec{V} \cdot \nabla\right)\vec{V}\right] + \frac{1}{f}\vec{k} \times \left(\omega \frac{\partial \vec{V}}{\partial p}\right) - \frac{1}{f}\vec{k} \times \vec{F_h} \ , \tag{3}$$

where ω is the vertical wind velocity, and p is the pressure. Decomposing the total wind velocity in the third term on the right-hand side of Equation 3, and using the thermal wind equilibrium equation $\vec{k} \times \frac{\partial \vec{V_g}}{\partial p} = \frac{R}{pf}\nabla_p T$, we obtain:

$$\vec{V}_a = \underbrace{\frac{1}{f}\vec{k} \times \frac{\partial \vec{V}}{\partial t}}_{LT} + \underbrace{\frac{1}{f}\vec{k} \times \left[\left(\vec{V} \bullet \nabla\right)\vec{V}\right]}_{IA} + \underbrace{\frac{R\omega}{pf^2}\nabla_p T}_{BE} \underbrace{- \frac{1}{f}\vec{k} \times \vec{F}_h}_{BLF} + \frac{1}{f}\vec{k} \times \left(\omega \frac{\partial \vec{V}_a}{\partial p}\right) \ , \tag{4}$$

where R is the gas constant and T is the temperature. Equation 4 is the diagnostic equation of the ageostrophic wind. There are five terms on the right-hand side: LT is the local tendency of total wind, IA is the inertial advection, BE is the baroclinic effects caused by the temperature gradient, BLF is the boundary layer friction term, and the fifth term is the vertical transport of the ageostrophic wind, which is calculated to be negligible compared to the previous four terms and will not be considered later. In this paper, we mainly focus on the ageostrophic winds at 925 hPa.

The LT term is the geostrophic deviation contributed by the unsteadiness of the wind field. The IA term is contributed by the advection of total wind, which is caused by the inhomogeneity of the wind along the direction of motion and the curvature of the streamline on the isobaric surface. The tangential and normal ageostrophic wind components of the streamline can be obtained by adhering to a natural coordinate system:

$$V_{sa2} = -\frac{1}{f}KV^2 \quad \text{and} \tag{5}$$

$$V_{na2} = \frac{V}{f}\frac{\partial V}{\partial s}, \tag{6}$$

where K is the curvature of the streamline.

The BE term refers to the geostrophic deviation contributed by the temperature gradient, which is proportional to the product of ω and the temperature gradient on the isobaric surface. This ageostrophic wind component appears in the case of horizontal temperature gradient and vertical motion. When there is vertical ascent, then the ageostrophic wind is consistent with the direction of $-\nabla_p T$.

The BLF term is mainly the ageostrophic wind component due to turbulence friction and vertical diffusion. In the northern hemisphere, this ageostrophic wind component is on the right side of $\vec{F_h}$ and perpendicular to it. Since there is no explicit solution for this term, the other five terms in Equation 4 are first calculated using reanalysis data, and then the value of BLF can be derived. Slater et al. (2014) proposed that the residual term of the horizontal momentum equation included errors arising from the time-interpolation and implicit horizontal diffusion of the model. Based on the analysis of Du et al. (2014), the residual term in their horizontal momentum model comprises friction, vertical advection, and other uncertainties, and the friction force dominates this term, and Luo et al. (2022) also used reanalysis data to calculate the friction term as the residual term. We use the data at 900 hPa and 950 hPa to obtain the vertical variation of ageostrophic wind in the last term at 925 hPa.

2.4 Two-dimensional Linear Horizontal Momentum Equation

To investigate the mechanisms underlying the diurnal variation of winds, we expand the simple 1D linear motion model of frictional flow on a f plane proposed by Du and Rotunno (2014) into a 2D model:

$$\frac{\partial u}{\partial t} - fv = -\frac{\partial \Phi}{\partial x} - \alpha u\ , \tag{7}$$

$$\frac{\partial v}{\partial t} + fu = -\frac{\partial \Phi}{\partial y} - \alpha v\ , \tag{8}$$

$$-\frac{\partial \Phi}{\partial x} = \overline{F_x} + \hat{F_x}[\,]\text{ , and} \tag{9}$$

$$-\frac{\partial \Phi}{\partial y} = \overline{F_y} + \hat{F_y}[\,]\ . \tag{10}$$

Here, (u, v) are wind components of (x, y) direction. $\alpha = \alpha_0[1 + \sin(t - t_0)\omega]$ is the diurnally varying frictional coefficient, which has a maximum at 1300 local standard times (LST, UTC = LST - 8hr) and a minimum at 0100 LST, and α_0 is the diurnal average. Three momentum tendency terms affect the total tendency of wind speed in this 2D model, including Coriolis force, pressure gradient force, and friction. The pressure gradient forces in the x and y directions have two parts: the mean $\left(\overline{F_x}, \overline{F_y}\right)$ and the diurnally varying $\left(\hat{F_x}[\,], \hat{F_y}[\,]\right)$ contributions, where [ ] has the form of $\cos\sigma t$ or $\sin\sigma t$ and σ is the diurnal frequency (2π day-1).

The numerical solution of the 2D model is

$$u^{t+\Delta t} = u^t + \Delta t\left(fv^t + \overline{F_x} + \hat{F_x}[\,] - \alpha u^t\right)\text{ and} \tag{11}$$

$$v^{t+\Delta t} = v^t + \Delta t\left(-fu^t + \overline{F_y} + \hat{F_y}[\,] - \alpha v^t\right). \tag{12}$$

α_0 is calculated using reanalysis data by way of Equations 7 and 8. The pressure gradient force input in the model is obtained by fitting the diurnal variation with the form of $\cos\sigma t$ or $\sin\sigma t$. The mean state of this term is calculated by the average of the heavy rainfall day. Its diurnal state is derived from the monthly mean during the whole of May to avoid the impacts of synoptic weather systems on diurnal variation (Luo et al., 2022).

In this 2D model, when the Blackadar mechanism is investigated individually, the diurnally varying component of the pressure gradient force is not considered, and only the diurnal mean value $(\overline{F_x}, \overline{F_y})$ is introduced into the model. When the Holton mechanism is considered individually, the diurnal variation of the friction coefficient should not be considered.

3 Overview of WSHR Cases

This paper selects two WSHR cases found by Huang et al. (2022) in South China, which occurred on 21-22 May 2013 and 16-17 May 2015, respectively. And referring to Huang et al. (2022), we define these two confluence patterns of the ageostrophic wind as confrontational confluence pattern and asymptotic confluence pattern, respectively. There are generally two main ageostrophic wind directions in the north and south sides of the rainfall area. If the difference between these two directions exceeds 120°, we define the confluence type of the ageostrophic wind as the confrontational confluence, otherwise, it is defined as the asymptotic confluence. We can clearly distinguish the two cases from Figure 3: Figure 3b shows that the directions of the ageostrophic winds on the north and south sides of the rainfall area in case 1 are almost opposite, presenting a confrontational pattern, so it is a confrontational confluence type. Figures 3c and 3b show that the angle between the north and south sides of the ageostrophic winds in case 2 is less than 120°. These two ageostrophic winds with similar wind directions gradually converge to the rain area, so it belongs to the asymptotic confluence type. Both cases occurred in similar synoptic situations without the influence of fronts in the lower troposphere.

3.1 Spatial Patterns and Temporal Variations of Rainfall

The rainfall of case 1 was mainly located in the central and eastern coastline of Guangdong Province (Figure 1a), with a large range of heavy rainfall centered in the PRD region, which showed a maximum of the 1-day total accumulated rainfall exceeding 300 mm. The rainfall covered about 500 km along the coastline. The rainfall of case 2 was mainly concentrated in the western coastal region of the PRD, and it covered about only 200 km along the coastline, with a maximum of the 1-day total accumulated rainfall exceeding 200 mm (Figure 1b). The blue rectangles in Figures 1a and 1b are the same selected rainfall areas, which cover most of the rainfall near the coastline in both cases. The center of heavy rainfall in case 1 was located roughly in the middle of the blue rectangle, and the rainfall in case 2 is located in the western half of the rectangle. We added up the hourly precipitation for all grid points in the blue rectangle. The maximum hourly accumulative rainfall in the blue rectangle in case 1 exceeded 12,000 mm (Figure 1c), and on 22 May 2013, it exceeded 4,000 mm from 0200 LST to 1700 LST. While in case 2, the maximum in case 2 was about 4,000 mm and the accumulative rainfall only exceeded 4,000 mm from 0800 LST to 1300 LST on 17 May 2015 (Figure 1d). The rainfall intensity in case 2 was weaker and shorter in duration than in case 1.

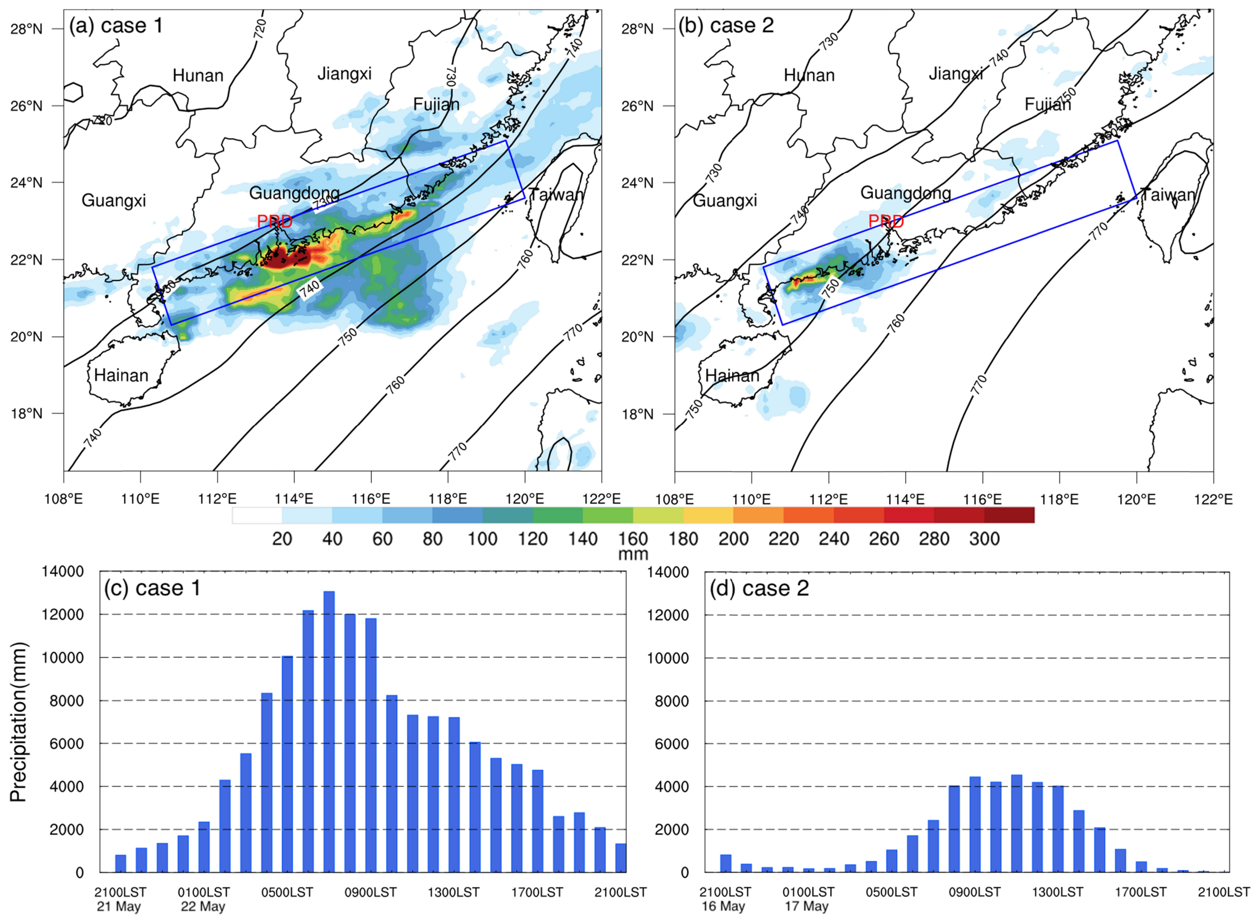

Figure 1. Total precipitation (shading) and mean geopotential height at 925 hPa (solid black line, at intervals of 10 gpm) for (a) case 1 from 2100 LST 21 May 2013 to 2100 LST 22 May 2013 and (b) case 2 from 2100 LST 16 May 2015 to 2100 LST 17 May 2015. The blue rectangle is the selected rainfall area for analysis. The latitudes and longitudes of the four corners of the blue rectangle are 20.3°N, 110.8°E, 21.8°N, 110.3°E, 25.1°N, 119.5°E, and 23.6°N, 120°E, respectively. (c)-(d) Variation of hourly precipitation in the blue rectangles in Figures 1a and 1b for (c) case 1 and (d) case 2.

3.2 Synoptic Conditions

In this section, we examine the synoptic conditions including large-scale atmospheric circulations, convergence, instability, and moisture conditions during these heavy rainfall events.

The large-scale atmospheric circulations show that both processes were influenced by troughs in the middle troposphere (Figures 2a and 2c), but the trough in case 1 was deeper, extending from central Hunan Province to northern Vietnam. The Western Pacific Subtropical High (WPSH) extended to the South China Sea (Figure 2a). Guangdong Province was located between the trough and the WPSH and was affected by strong southwesterly jets. While in case 2, there was only a short-wave trough in eastern Guangxi, and the WPSH was located east of 125°E, so the southwesterly flow ahead of the trough was weaker. The synoptic patterns of the two cases at 850 hPa were similar (Figures 2b and 2d). Geopotential heights were generally higher in the northwest and lower in the southeast. There was no apparent influence of synoptic fronts in either case. The patterns at 925 hPa in Figures 1a-b, and Figure 3 show the isobaric distribution in the two cases was similar, and there was a southwesterly BLJ over the southern part of the precipitation area. While the range of the BLJ at 925 hPa in case 1 was larger, extending to the east of Fujian, its wind velocity was also stronger than in case 2, with the velocity at the jet axis generally exceeding 12 m s^{-1} (Figure 3). In case 2, the region of the BLJ was mostly confined to the southern part of the PRD.

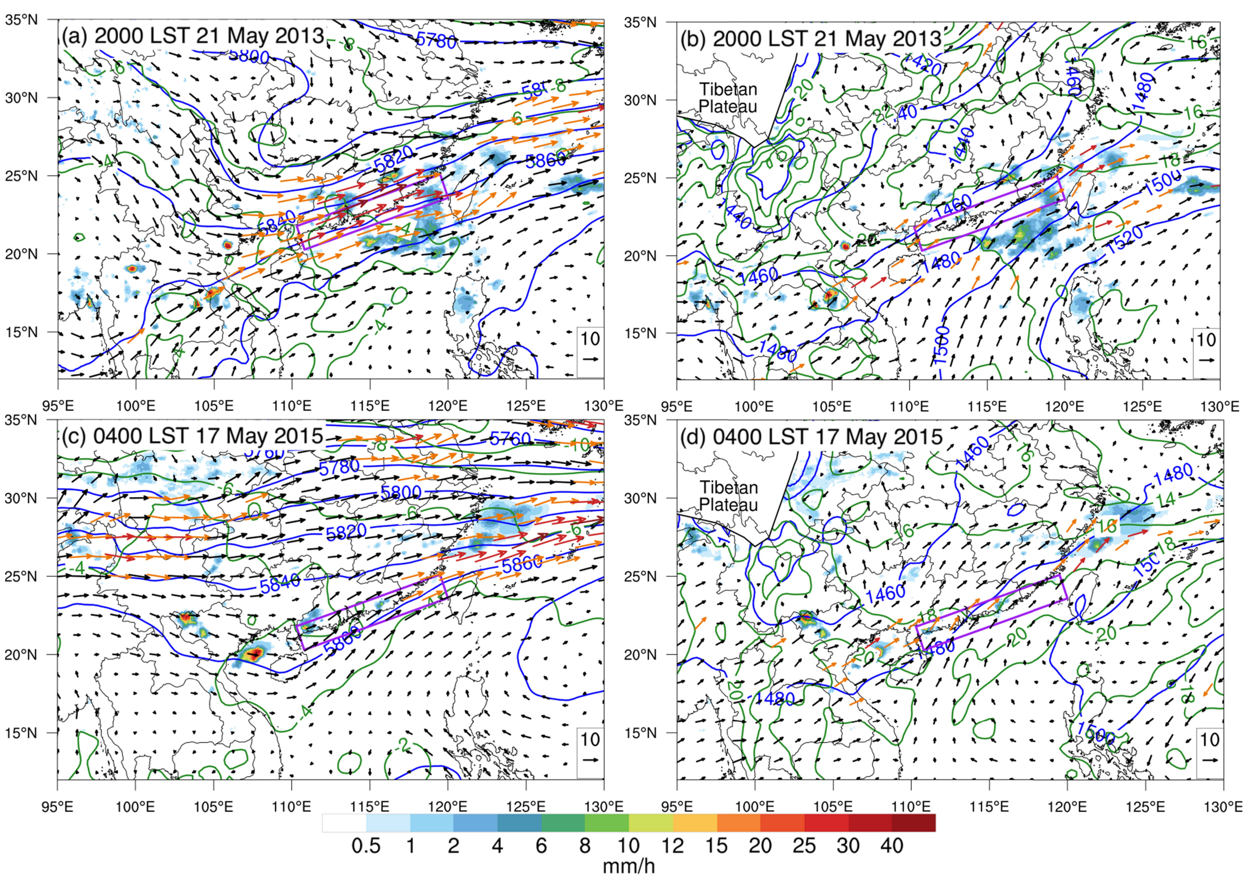

Figure 2. Synoptic patterns at (a, c) 500 hPa and (b, d) 850 hPa at (a, b) 2000 LST 21 May 2013 and (c, d) 0400 LST 17 May 2015, with the blue and green solid lines representing the geopotential height at intervals of 20 gpm and the temperature at intervals of 2°C, with shading representing the hourly precipitation (mm). The brown, red, and orange vectors represent (a, c) total winds with speeds of higher than 25 m s^{-1}, 20 m s^{-1}, and 15 m s^{-1}, respectively, and (b, d) total winds with speeds of higher than 15 m s^{-1}, 12 m s^{-1}, and 10 m s^{-1}, respectively. The solid black line represents the area with a terrain height exceeding 3000 m. The purple rectangles are the same areas as the blue rectangles in Figures 1a and 1b.

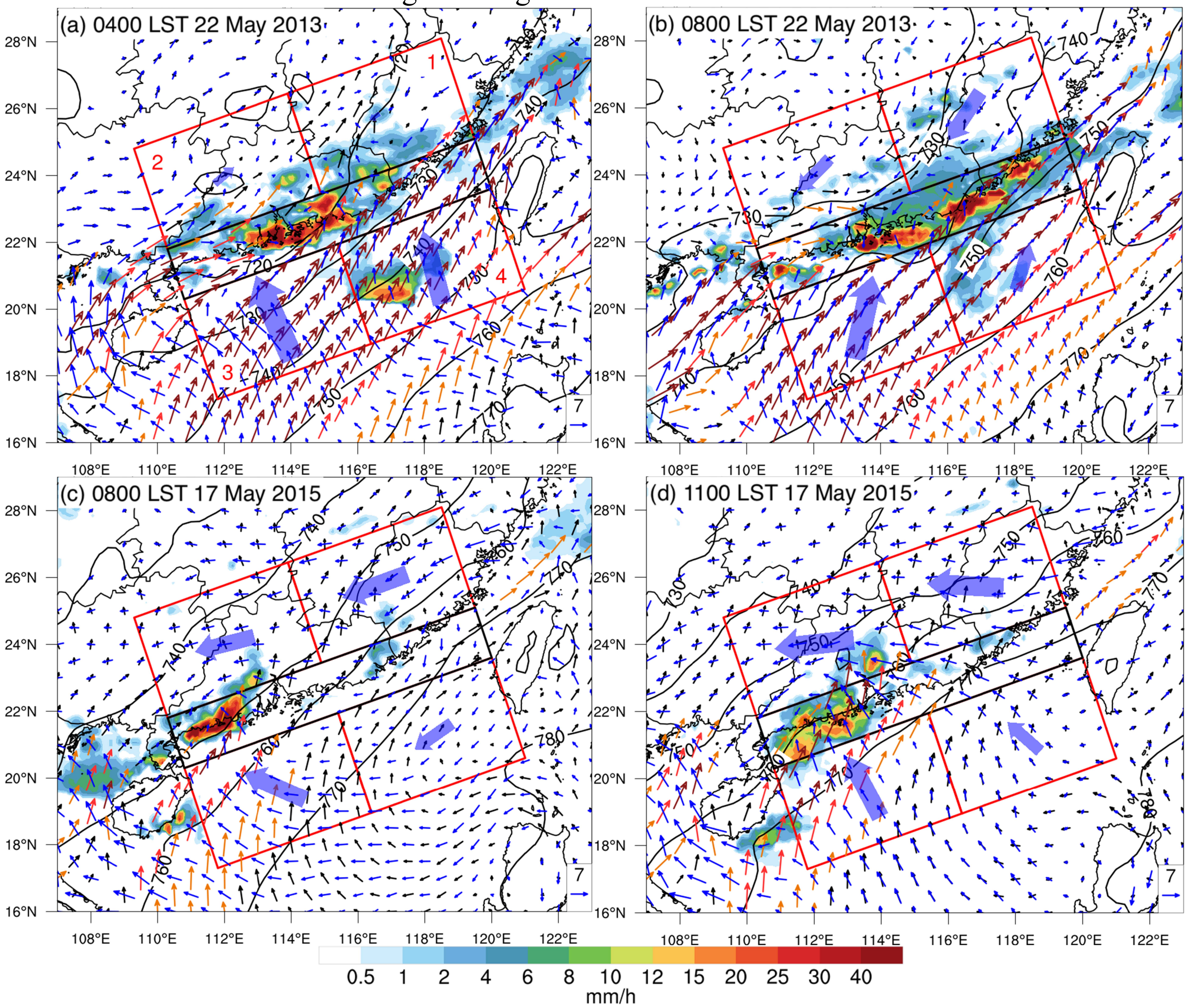

Figure 3. Synoptic patterns at 925 hPa at a certain moment during the occurrence of (a, b) case 1 and (c, d) case 2, with the solid black lines representing the geopotential height at intervals of 10 gpm, the shading representing the hourly precipitation (mm), and the blue vectors representing the ageostrophic winds. The brown, red, orange, and black vectors represent total winds with speeds of higher than 12 m s^{-1}, 10 m s^{-1}, 8 m s^{-1} and lower than 8 m s^{-1}, respectively. The black rectangles are the same areas as the blue rectangles in Figures 1a and 1b. The red rectangles are the selected areas for analyzing the winds. The larger blue translucent arrows represent the regionally-averaged ageostrophic winds in the four red rectangles, with their

thickness and length representing the magnitude of the ageostrophic winds. The region without values is that with topographic height above geopotential height at 925hPa.

The spatial distributions of the horizontal divergence at 925 hPa (Figure 4) show that in case 1, there was a band of convergence near the coast of Guangdong Province, and there was also a region with a large value of convergence in the western part of Guangdong coastline in case 2, which were both located at the termini of the southwesterly BLJs. Figures 4c-d show the variations of the sum of the horizontal divergence in the black rectangle in Figures 4a-b. The horizontal divergence in the rainfall area was generally negative before and during the heavy rainfall in the lower troposphere, which represents the dynamical lifting conditions by continuity. In case 1, the divergence reached its minimum value at 0700LST on 22 May 2013. While the minimum value of case 2 was much larger than that of case 1, indicating that the convergence in case 1 was wider and stronger than in case 2.

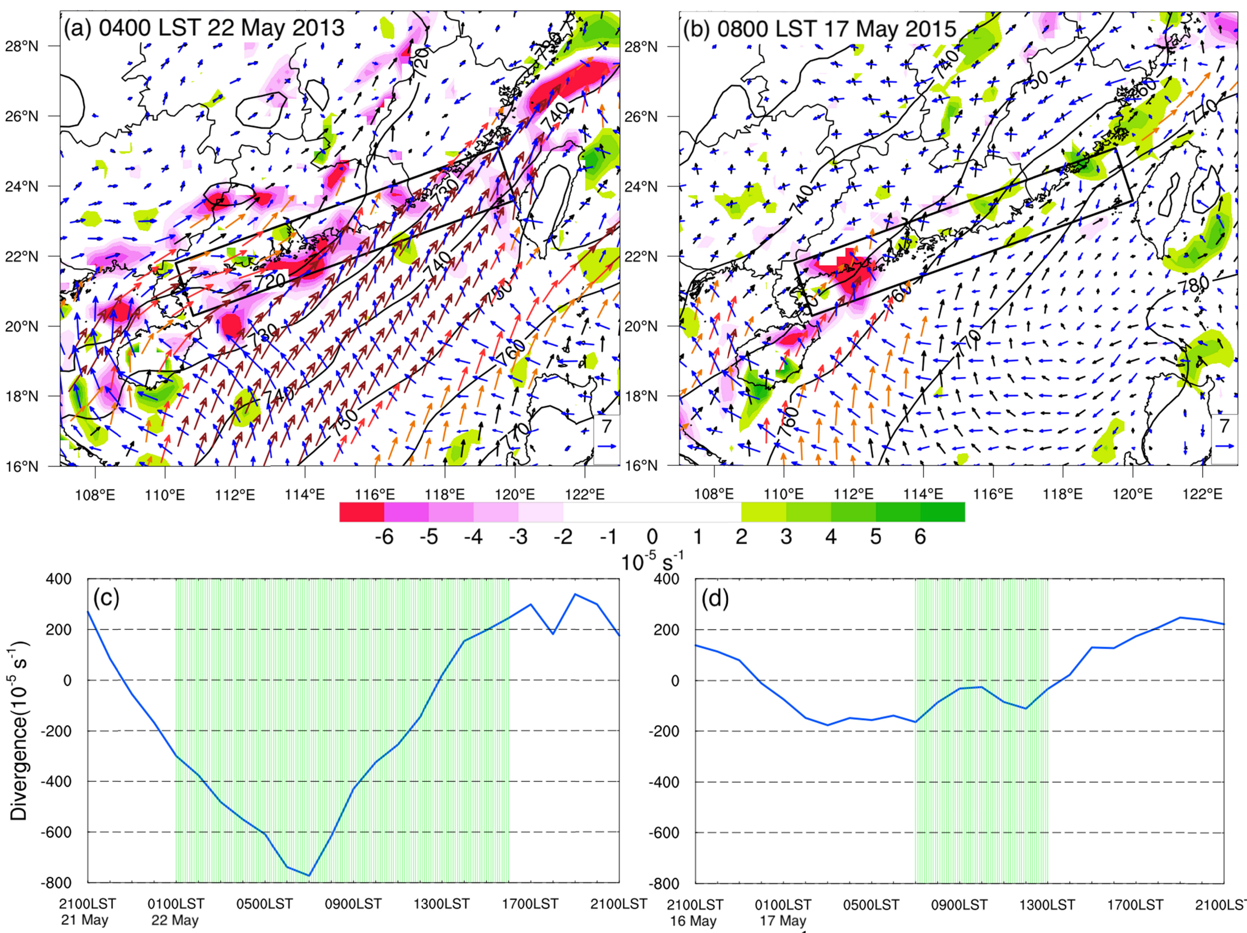

Figure 4. Spatial distributions of the horizontal divergence (s^{-1}, shading) at 925 hPa of (a) case 1 and (b) case 2, with the synoptic patterns set as Figure 3. Hourly variations of the sum of the horizontal divergence at 925 hPa in the black rectangle of (c) case 1 and (d) case 2, with the

green shading showing the time when the hourly accumulated precipitation exceeds 4,000 mm in the black rectangle.

Figure 5 shows the spatial distributions of the most-unstable CAPE and moisture flux and its convergence during heavy rainfall. The spatial patterns of moisture flux were similar to the low-level winds (Figures 3 and 5). In case 1, there was a wide range of moisture flux convergence in Guangdong and Fujian province, especially in the coastal region, which was favorable for heavy rainfall (Figures 5a and 5b). And in case 2, the areas with strong moisture flux convergence also corresponded well with the rainfall areas (Figures 5c and 5d and Figures 3c and 3d). The maximum value of CAPE was located at sea around Hainan province, where for the most part it exceeded 800 J kg^{-1} in the rainfall areas in both cases (Figure 5), leading to favorable conditions for heavy rainfall.

These results demonstrate that both rainfall events were located in the terminus of the BLJs near the coastline, with abundant moisture from the South China Sea, strong convergence that represents low-level lifting, and convective instability, which are three ingredients contributing to rainfall (Doswell et al., 1996). While the intensity and extent of BLJs differed in the two cases, the horizontal convergence and moisture flux convergence in the lower troposphere were both stronger in the confrontational confluence type case than the asymptotic confluence type case, likely contributing to the heavier intensity and longer duration of rainfall. Moisture flux convergence can be mostly attributed to the convergence of winds, that is, the convergence of ageostrophic winds, so the distribution of the ageostrophic winds and their confluence modes are important factors in WSHR events.

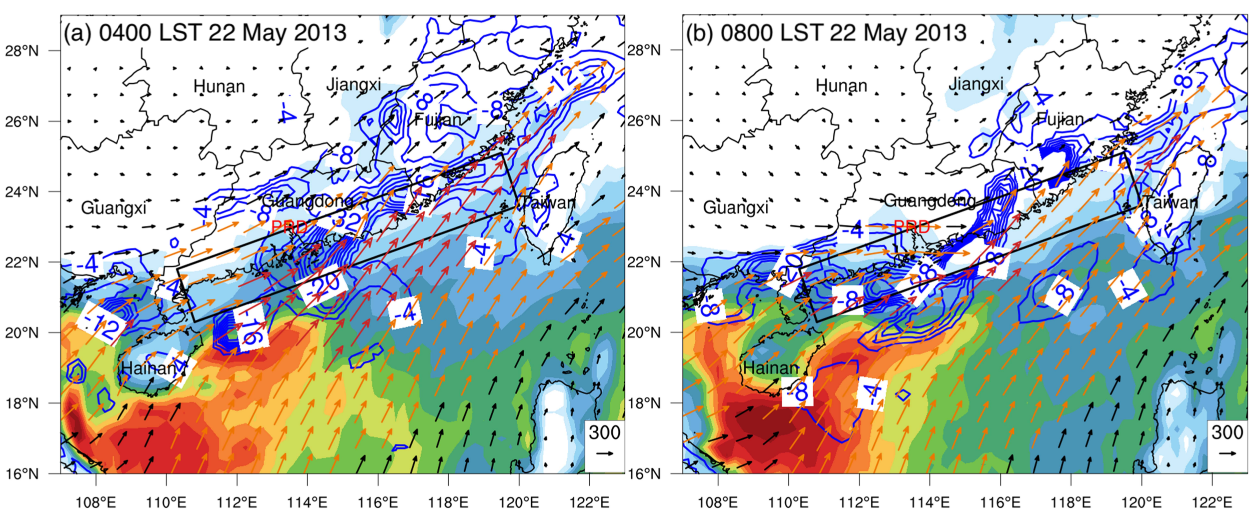

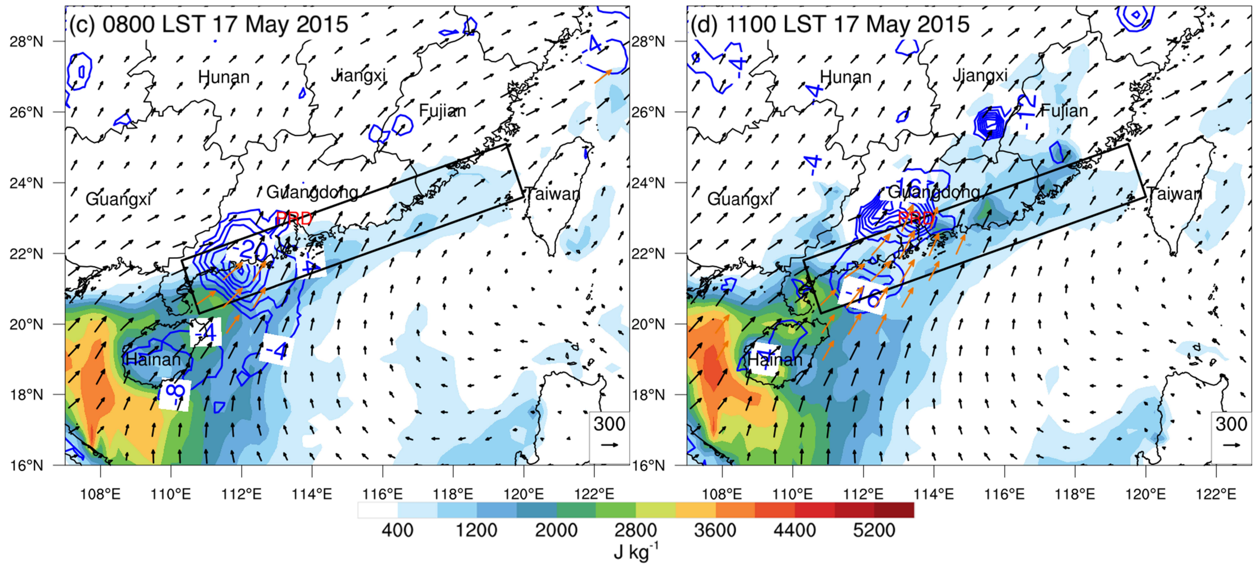

Figure 5. Spatial distributions of the moisture flux by total winds (kg m^{-1} s^{-1}, vectors), horizontal moisture flux divergence (10^{-4} kg m^{-2} s^{-1}, contour lines), and most-unstable CAPE (J kg^{-1}, shading). The red, orange and black vectors represent higher than 600 kg m^{-1} s^{-1}, 400 kg m^{-1} s^{-1}, and lower than 400 kg m^{-1} s^{-1}, respectively, and the contour lines are from -32 to -4 at intervals of 4. All of these fluxes are vertically integrated from 1000 hPa to 700 hPa.

4 Ageostrophic Wind Patterns and Diagnosis Results

As shown in Section 3, differences exist in the convergence intensity in the lower troposphere in these two cases. The spatial distribution and temporal variations of ageostrophic winds and their diagnosis results are examined in this section. The four red rectangular areas in the north and south sides of the rainfall area, shown in Figure 3, are selected as the four quadrants, and the first, second, third, and fourth quadrants are in counterclockwise order starting from the northeastern red rectangle. The width of these red rectangles is consistent with the width of the selected rainfall area, and the direction of total and ageostrophic winds in each quadrant is mostly consistent. The first two quadrants are located on land, and the third and fourth quadrants are located at sea. The following analysis in case 1 focuses on these four quadrants, while in case 2 we focus on the second and third quadrants since the rainfall was located between these two quadrants.

4.1 Spatial Distribution and Temporal Variations of Ageostrophic Winds

The distribution of ageostrophic winds in the four quadrants in Figure 3 and the diurnal variation of ageostrophic winds in Figure 6 show that during these two WSHR processes, the ageostrophic winds in the first and second quadrants were mostly easterly or northeasterly, and the diurnal variation of wind direction in these two quadrants was not distinct. The difference between the two cases was confined mainly to the third and fourth quadrants at sea. The ageostrophic winds in case 1 had a notable clockwise rotation trend after nightfall, which changed from southeasterly ageostrophic winds in the early period of precipitation to southwesterly winds (Figures 3a, 3b, and 6a), which was likely due to the inertial oscillation in the boundary layer. And at 0700 LST on 22 May 2013, the horizontal divergence in the rainfall area was at its minimum (Figure 4c). During the period represented by the bold wind vector in Figure 6a from 0300 LST to 1500 LST on 22 May 2013, the angles between the ageostrophic winds in the first two quadrants and the last two quadrants mostly exceeded 120°. At 0900 LST and 1200 LST, the angles were even close to 180°, which is more clear in Figure 3b, resulting in the formation of a confrontational confluence pattern. During this time, the total hourly precipitation in the blue rectangle exceeded 4000 mm (Figure 1c), and the hourly precipitation range at 0800 LST on 22 May was larger than that at 0400 LST (Figures 3a and 3b), which extended to the south of Fujian with greater intensity. The periods of the heaviest rainfall correspond to when the ageostrophic winds on the north and south sides are most confrontational, which coincides with the greatest convergence (Figure 4c). The variation of ageostrophic winds after nightfall at sea in case 2 was not notable, and they mostly maintained southeasterly (Figure 6b). Even during the heavy rainfall period from 0900 LST to 1200 LST on 17 May 2015, the angle between the two sides was smaller than 120°, and the wind velocity was also weaker than that in case 1, and Figure 4d shows less value of horizontal convergence. Therefore, the asymptotic confluence pattern was the result, and the precipitation intensity had no notable change (Figures 1d, 3c, and 3d).

The distribution of the ageostrophic winds mainly had two characteristics in the two cases. First, in both cases, the diurnal variation of the ageostrophic wind direction on land was not distinct compared with that at sea, so the diurnal variation phase difference of ageostrophic winds between the sea and land led to the convergence in the rainfall area. Second, over the sea, the diurnal variation of ageostrophic winds was more distinct in case 1 than in case 2, the characteristic of inertial oscillations after nightfall was more obvious, and the ageostrophic wind velocity was also stronger, which led to confrontational confluence in case 1 and asymptotic confluence in case 2. We will analyze the reasons for these behaviors of ageostrophic winds with diagnostic results.

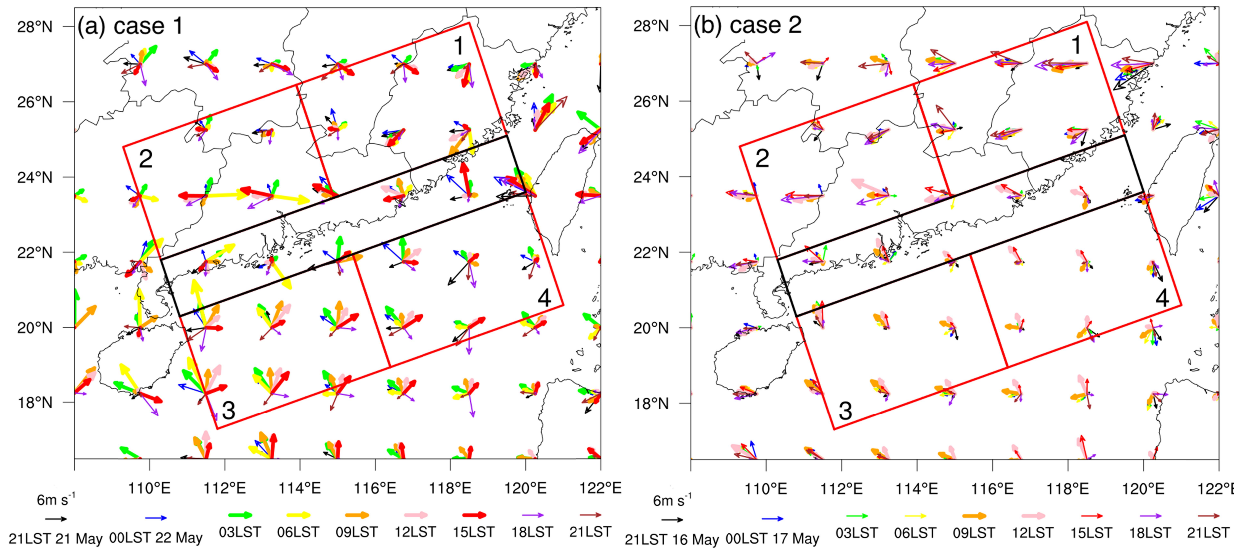

Figure 6. Horizontal distribution of diurnal variation of ageostrophic winds at 3-h intervals at 925 hPa during heavy precipitation in (a) case 1 and (b) case 2, with the bold vectors representing the time when the regional hourly precipitation within the black rectangle exceeded 4000 mm. The region without values is that with topographic height above geopotential height at 925hPa.

4.2 Diagnosis Results of Ageostrophic Winds

To investigate the mechanisms of the land-sea contrast in the diurnal variation of ageostrophic winds and the differences in the diurnal variation at sea between the two cases, this section focuses on the diagnostic analysis of the LT, IA, BE, and BLF terms that constitute ageostrophic winds.

Figure 7 shows that in the first and second quadrants of case 1, the ageostrophic wind components of the IA term and the BE term were weaker compared to the other two terms and could be ignored. The LT term contributed some diurnal variation in the direction of the ageostrophic winds, but its wind speed was weaker than the BLF term. The BLF term contributed northeasterly and easterly ageostrophic winds in the first and second quadrants, which was consistent with the total ageostrophic winds (Figure 6a), indicating that the ageostrophic winds on land were due principally to surface friction.

For the third and fourth quadrants of case 1, the ageostrophic wind component of LT term was strong, and the wind direction had a distinct clockwise rotation trend after nightfall from

2100 LST on 21 May 2013 (Figure 7a). It was consistent with the variation of the total ageostrophic winds, while the southwesterly ageostrophic wind component in the third quadrant from 0900 LST to 1200 LST on 22 May 2013 was weaker than the total ageostrophic winds (Figures 6a and 7a). The IA term component was stronger in places with large total wind speed gradients, such as the east of Hainan and the Taiwan Strait. The component in the third quadrant was mostly stronger than that in the fourth quadrant, and the southerly and westerly ageostrophic winds from 0300 LST to 1200 LST on 22 May 2013 positively contributed to the total ageostrophic winds. The BE component was mainly located in areas with larger temperature gradients. It was weaker and was almost southerly, which contributed to the convergence. The BLF component was as strong as LT term at sea, which had irregular diurnal variation, it could contribute easterly and southeasterly ageostrophic winds at some times and locations.

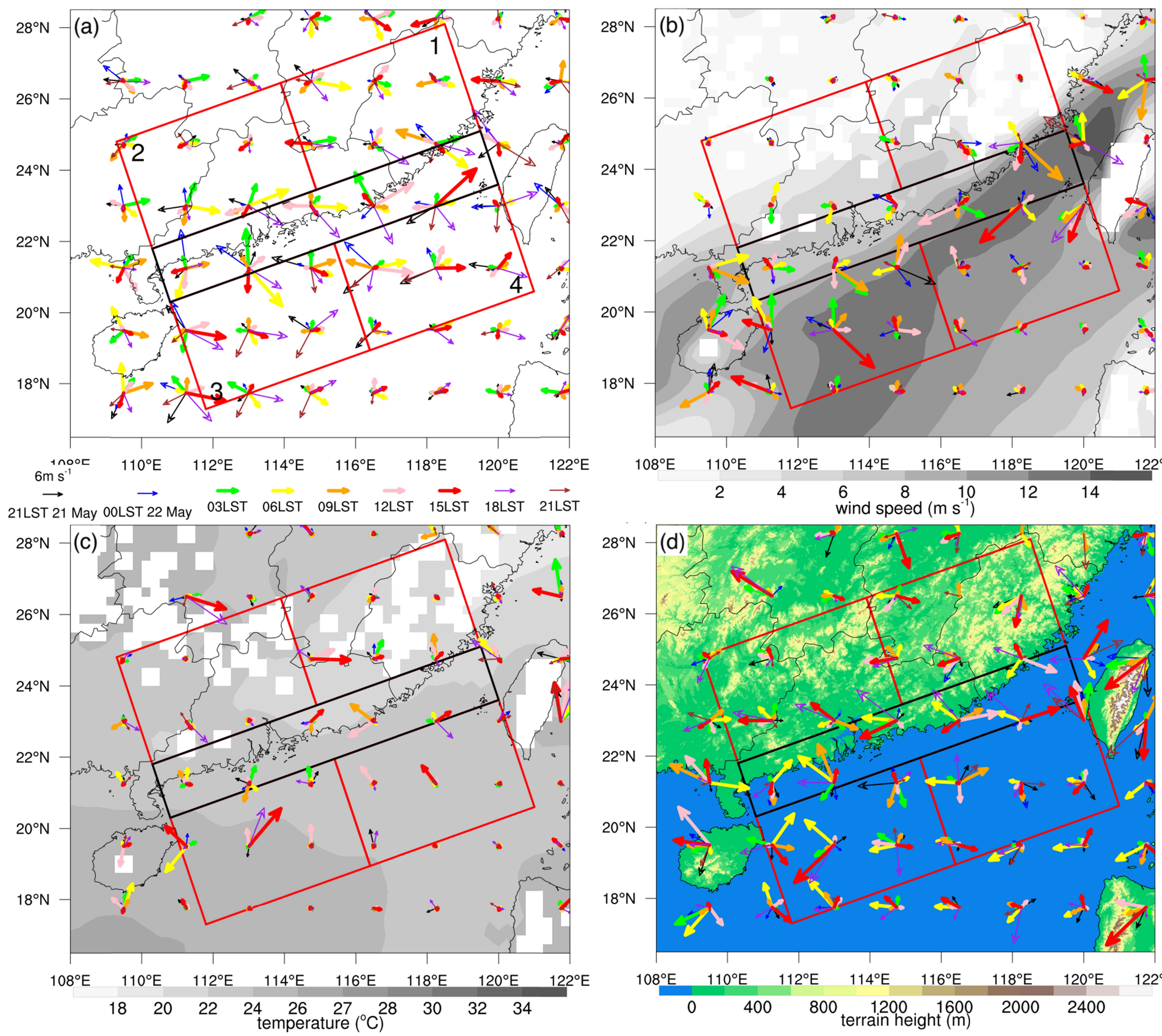

Figure 7. Horizontal distribution of diurnal variation of ageostrophic winds at 3-h intervals at 925 hPa contributed by the (a) local tendency of total wind (LT) term, (b) inertial advection (IA) term, (c) baroclinic effect (BE) term, and (d) boundary layer friction (BLF) term in case 1, with the bold vectors representing the time when the regional hourly precipitation within the black rectangle exceeded 4000 mm. The shading in Figures 7b, 7c, and 7d represent the average total wind velocity, average temperature from 2100 LST 21 May 2013 to 2100 LST 22 May 2013 at 925 hPa, and the topographic height, respectively. The region without values is that with topographic height above geopotential height at 925hPa or 950 hPa.

Figure 8 shows that the composition of the ageostrophic winds on land in case 2 was very similar to that in case 1: the BLF term contributed strong northeasterly and easterly ageostrophic winds in the first and second quadrants. In the third and fourth quadrants, the ageostrophic wind speed contributed by the LT term was comparable to that by the BLF term, which was weaker than that in case 1, and the diurnal variation is not as significant as that in case 1. There was almost no southwesterly ageostrophic wind before 1200 LST on 17 May 2015, when the heavy rainfall was coming to an end. The IA term and BE term contributed weak ageostrophic winds at sea, which could be neglected. The BLF term contributed easterly and northeasterly ageostrophic winds in the third and fourth quadrants, and the wind speed is weaker than that on land.

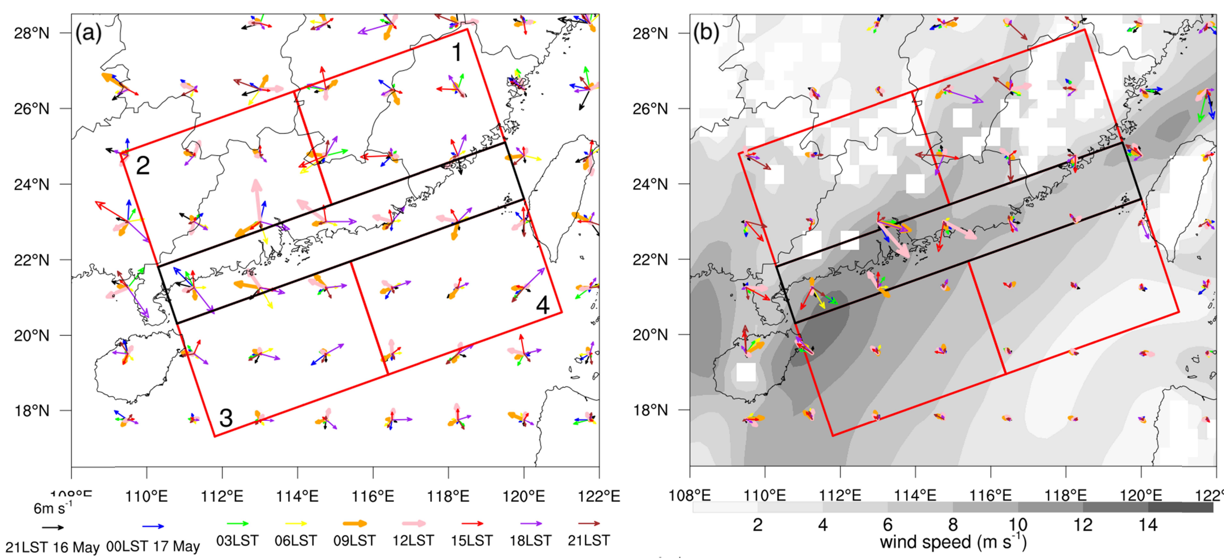

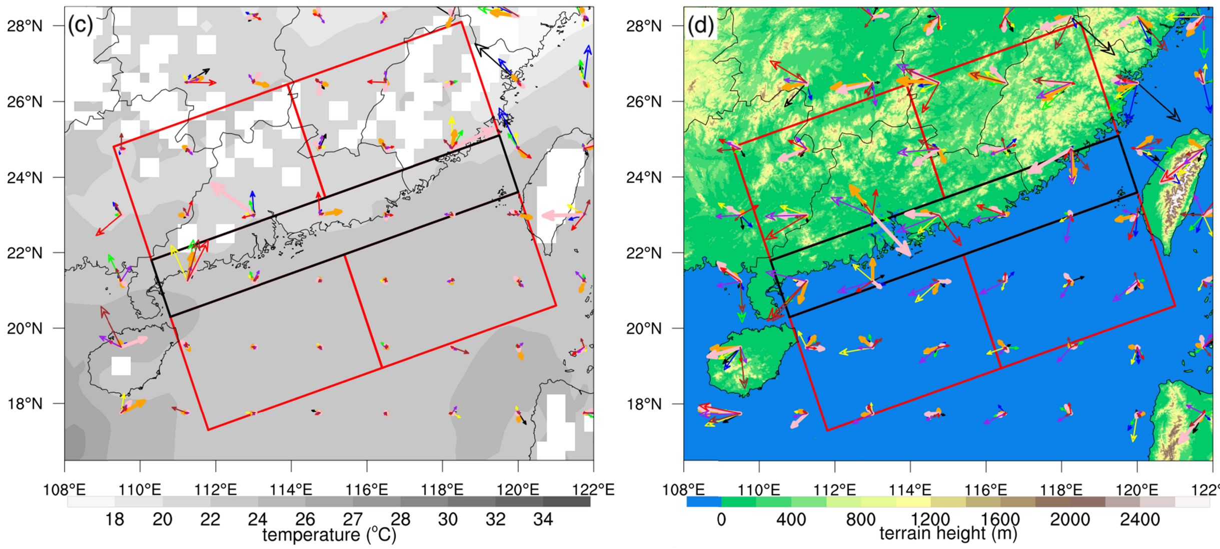

Figure 8. As in Figure 7, but for case 2 and the average values from 2100 LST 16 May 2015 to 2100 LST 17 May 2015.

In the two cases, on land, the BLF term dominated the easterly and northeasterly ageostrophic wind components. Although the LT term contributed some of the diurnal variation in the ageostrophic wind direction, its wind velocity was not strong enough to cause a significant diurnal variation in the total ageostrophic wind direction. In contrast, at sea, the contribution of the LT term was greater, resulting in significant diurnal variation in the total ageostrophic wind direction, deflecting it southeasterly or even southwesterly. Since the winds at sea were mainly the BLJs, the LT terms actually represented the diurnal variation of the BLJs. The diurnally varying phase difference between the sea and land generates the convergence of ageostrophic winds in the north and south. The difference between the two cases at sea was due to the combined effect of the four terms. They contributed southwesterly ageostrophic wind at sea in case 1 and formed a confrontational confluence pattern with the northeasterly ageostrophic wind on land, resulting in precipitation with a wider spatial range and heavier intensity.

5 The Physical Mechanisms of the Four Diagnosis Terms

The contributions of the four diagnosis terms in the lower troposphere had been examined in the previous section. This section will focus on the physical mechanisms of the terms and the reasons for the difference in confluence modes between the two cases.

5.1 The Mechanisms of LT Term

The previous section shows that the ageostrophic wind component of the LT term is characterized by an inertial oscillation at night, especially in case 1, while the other three terms are not. This can be explained by Equation 4: The inertial oscillation mechanism is established under the assumptions that the horizontal pressure gradient force is constant with time, the motion is horizontal, and there is no friction at night (Blackadar,1957). After simplifying Equation 4 using these assumptions, only LT and IA terms are left on the right side, and the component of IA is relatively weaker, so the inertial oscillation is reflected in the LT term.

Since the effect of the LT term was more notable at sea, and its difference between the two cases was mainly in the third and fourth quadrants, only the winds in the last two quadrants in case 1 were discussed in this section. And for case 2, the rainfall area was between the second and third quadrants, so we only focus on the winds in the third quadrant in case 2. The LT term is mainly caused by the unsteadiness of wind, so the different behaviors of the LT term indicate the difference in the diurnal variation of the total wind between the two cases. In both cases, the winds offshore were mainly the BLJs, so the diurnal variation of the BLJs had differences.

The boundary layer friction variation will affect the diurnal variation of BLJ through the Blackadar mechanism. In addition, the rainfall region is located in the coastal area of South China, and there is a diurnal variation of thermal forcing because of the difference in thermal properties between the ocean and land. Therefore, the Holton mechanism also has an impact on the diurnal variation of BLJ in this region. This paper used a simple 2D model to analyze the relative contribution of these two mechanisms. Figures 9a–d and 10a–d show that the individual momentum tendency terms of Equations 7 and 8 calculated by the ERA5 reanalysis data agreed with those obtained from the combined 2D model simulation. It indicates that the combined 2D model could reproduce the momentum budget very well and thus could be used for subsequent analysis.

Figures 9e and 9f show that the peak regional average u-component of the wind in case 1 occurred at 1600 LST on 22 May 2013, and the peak v-component occurred at 0400 LST on 22 May 2013, and both components had great diurnal variations. The difference between the maximum and minimum values of the v-component was about 9 m s^{-1}, thus, it could generate a strong local wind speed tendency. From the LT term in Equation 4, the u-component of ageostrophic wind of this term is $-\frac{1}{f}\frac{\partial v}{\partial t}$, and the v-component is $\frac{1}{f}\frac{\partial u}{\partial t}$. Therefore, from 0400 LST 22 May 2013, when the v-component of the total wind speed reached its peak until 1600 LST when the u-component reached its peak, both u- and v-components of the ageostrophic wind were positive, so the regional average ageostrophic winds contributed by the LT term were southwesterly, noting this period also corresponded to the stage of heavy precipitation. Figures 10e and 10f show that in case 2, the diurnal variation of the average u- and v-components of the total wind speed was relatively weak, especially for the u-component. The peak of the v-component occurred at about 1400 LST. During the heavy rainfall, both u and v components increased slightly with time, so the LT term could only contribute southeasterly ageostrophic winds, thus causing an asymptotic confluence pattern.

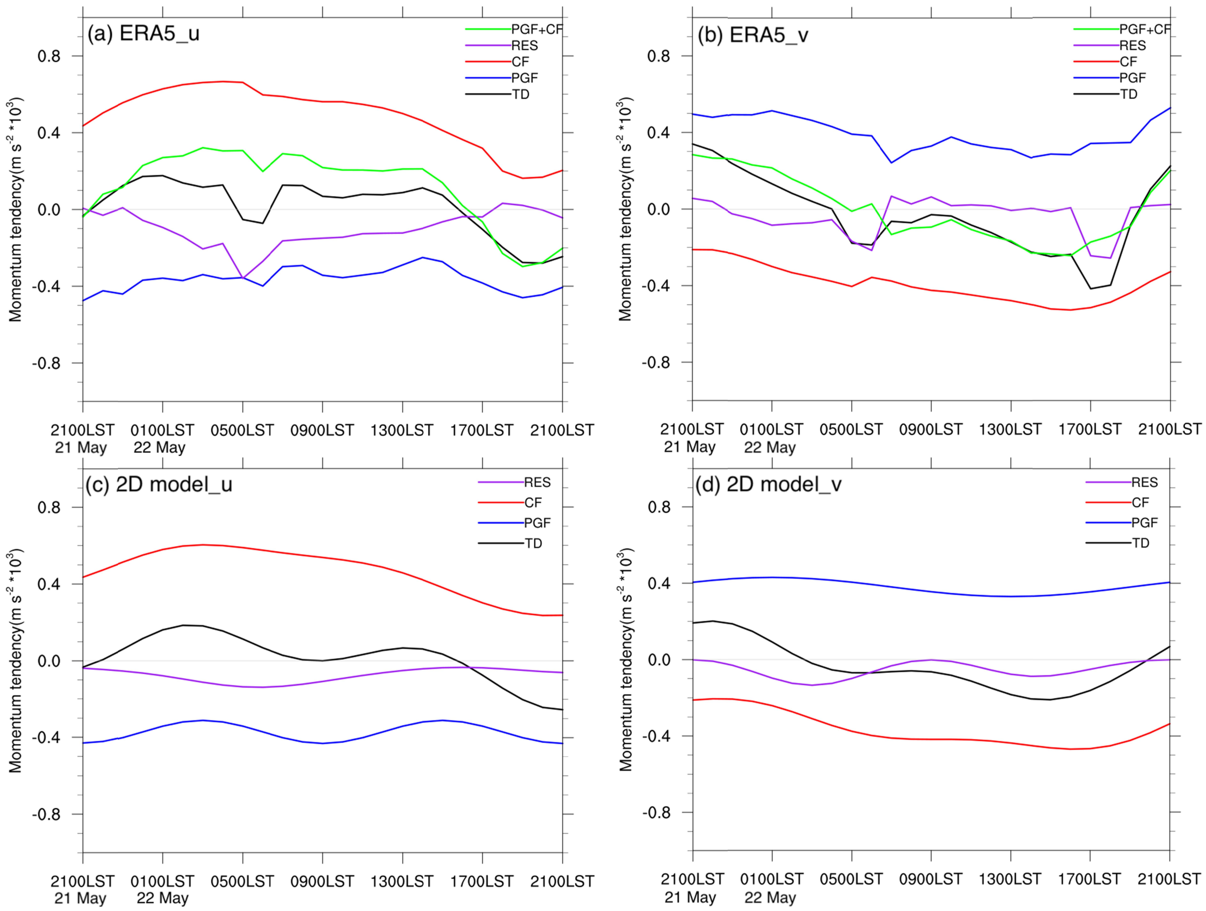

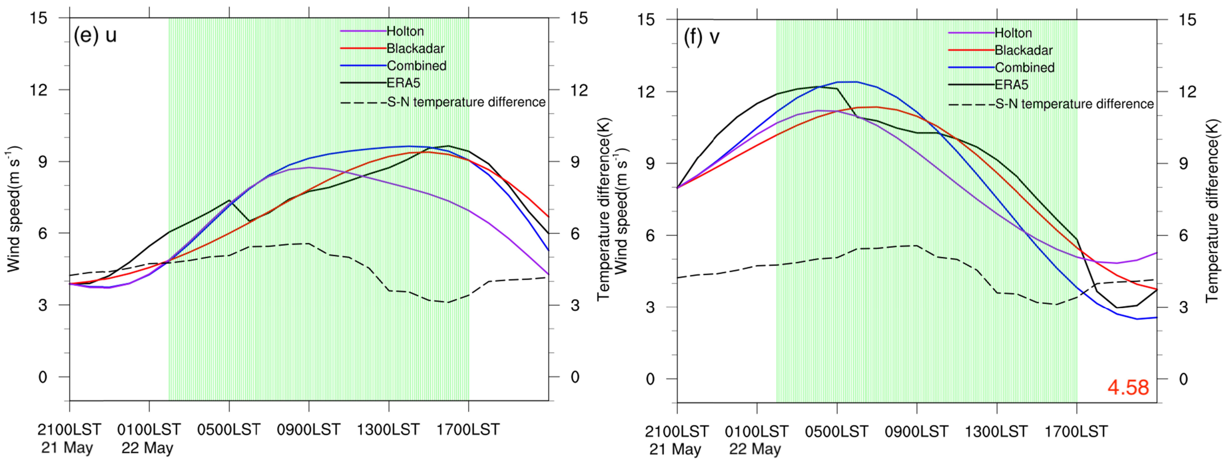

Figure 9. Diurnal variations of the regionally-averaged total tendency of wind speed (TD), pressure gradient force (PGF), the Coriolis force (CF), and friction (RES) terms in the (a) zonal and (b) meridional directions of the horizontal momentum equations at 925 hPa in the third and fourth quadrants from the ERA5 reanalysis data in case 1, with each term magnified by a factor of 1,000, and (c, d) the corresponding terms from the simple 2D model. The diurnal variation of the regional average of (e) zonal wind and (f) meridional wind, with the solid black lines representing the results from ERA5 reanalysis data, the solid red lines representing the simulation results from the pure Blackadar mechanism, the solid purple lines representing the simulation results from the pure Holton mechanism, and the solid blue lines representing the simulation results from the combined mechanism using the 2D model. The dashed black lines in Figures 9e and 9f represent the variation of the average 2-m temperature difference (K) between the southern boundary of the third and fourth quadrants and the southern boundary of the first and second quadrants in Figure 1a. The green shading shows the time when the hourly accumulated precipitation exceeds 4,000 mm in the blue rectangle in Figure 1a. The number in the lower right corner of Figure 9f is the mean value of the average 2-m temperature difference during that period, as shown by the green shading.

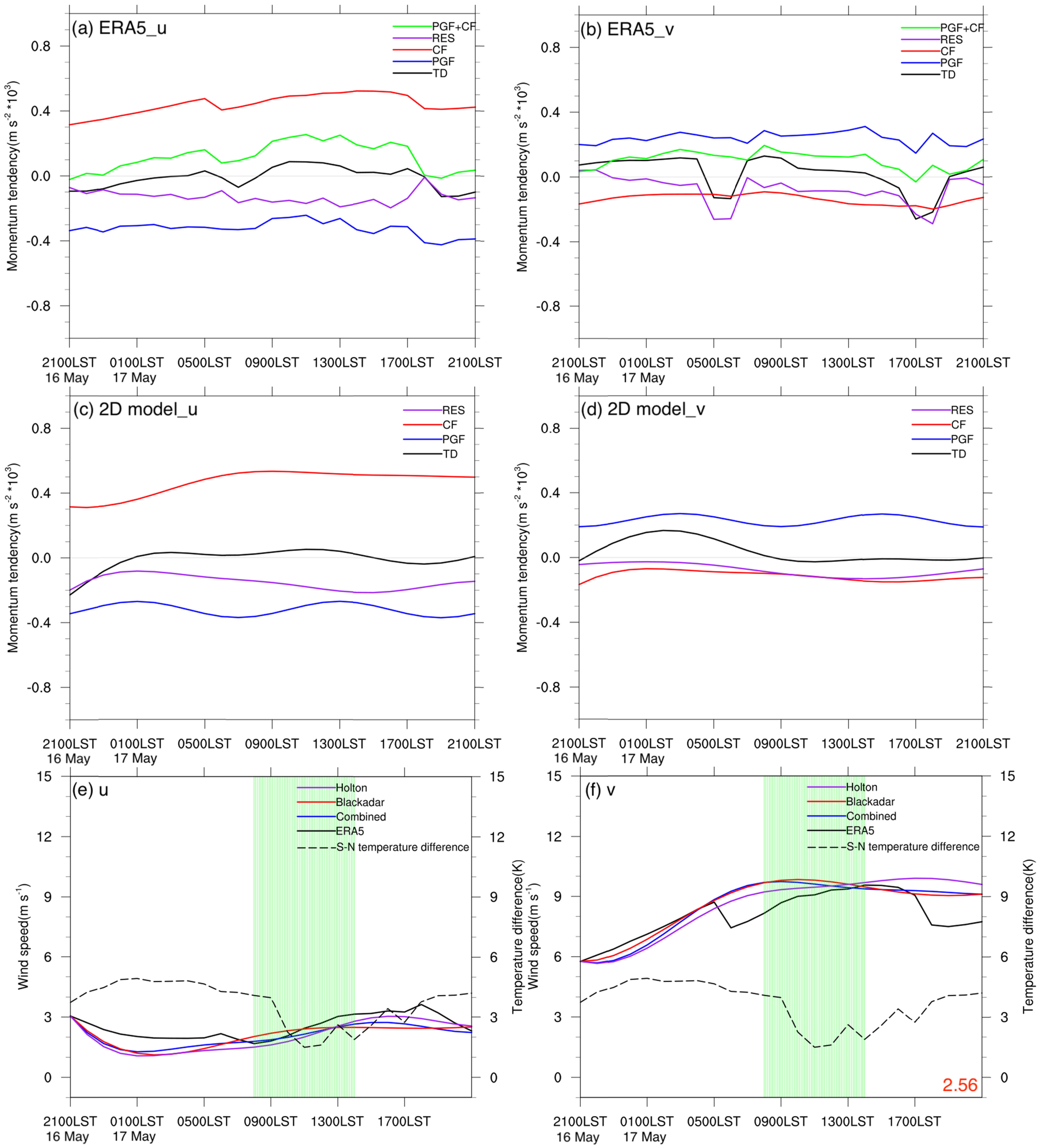

Figure 10. As in Figure 9, but for case 2, the dashed black lines in Figures 10e and 10f represent the variation of the average 2-m temperature difference between the southern boundary of the third quadrant and the southern boundary of the second quadrant in Figure 1b.

The mechanism responsible for the difference in the diurnal variation of the total wind between the two cases is discussed below by comparing the reanalysis data and the results simulated by the 2D model. For the u-component of case 1, the peak of the pure Blackadar mechanism result was closer to the ERA5 result (Figure 9e), and the magnitude of the wind speed was also similar, while the pure Holton mechanism resulted in an earlier peak of about 7 hours. For the v-component (Figure 9f), the peak of the pure Holton mechanism appeared almost at the same time as the ERA5 result at about 0400 LST. The peak of the pure Blackadar mechanism was also close to reality with about 2 hours later. This indicated that for case 1, the pure Blackadar mechanism scenario could well simulate the diurnal cycle of winds in both directions. Figures 9a and 9b show that after night, the total tendency was consistent with the sum of pressure gradient force and Coriolis force in both directions, which suggested the boundary decoupled during the night due to surface cooling. Accordingly, the Blackadar mechanism played important role in the diurnal variation of the BLJ in case 1, making the v-component reach its maximum in the early morning.

For case 2, the effect of the pure Holton mechanism on the u-component was closer to reality. The peak of the pure Blackadar mechanism was not distinct (Figure 10e). The v-component in the Holton mechanism approached its maximum at about 1700 LST, delaying about 2 hours compared to reality, while the peak of the Blackadar mechanism appeared about 5 hours earlier. The diurnal variation of the v-component of the pure Holton mechanism was also constant with the reanalysis data. Figures 10a and 10b show that the boundary decoupling at night was not significant in case 2. Therefore, the Holton mechanism dominated the diurnal variation of the BLJ in case 2, that is, the land-sea thermal forcing had a more important effect.

To investigate the thermal difference between land and sea in the two cases, the difference in temperature at 2 m between the southern boundary of the third and fourth quadrants and the southern boundary of the first and second quadrants was calculated for case 1 (Figure 9f), and the difference between the southern boundary of the third quadrant and the southern boundary of the second quadrant was calculated for case 2 (Figure 10f). In case 1, the temperature difference was maintained above 3 K throughout the day, and the average difference reached 4.58 K when the regional cumulative hourly precipitation exceeded 4000 mm. In case 2, the difference was generally smaller, and the average temperature difference during heavy precipitation was only 2.56 K. The minimum difference appeared at 1100 LST due to the warming by solar radiation on land. When the temperature on land increases, the meridional sea-land thermal difference decreases, and the low-level thermal circulation will weaken, which is conducive to the strengthening of southerly winds. The temperature on land was closer to that at sea at noon in case 2, so the v-component could get stronger in the afternoon. This verified that the thermal difference between the sea and land surface plays a more important role in case 2 than in case 1 during the WSHR.

The Blackadar mechanism and Holton mechanism dominate the diurnal variation of BLJs in case 1 and case 2, respectively, resulting in the maximum wind speed in case 1 and case 2 appearing in the early morning and afternoon, respectively. Therefore, the behaviors of LT term in these two cases were different. The diurnal variation of the boundary layer friction and the land-sea thermal contrast dominate the LT term in case 1 and case 2, respectively, thus influencing the ageostrophic winds.

5.2 The Mechanisms of IA Term

Since the IA term is the geostrophic deviation contributed by the advection of total wind, Equation 4 also shows that this term is proportional to the total wind speed and its gradient, so a different horizontal distribution of total wind will cause a difference in the ageostrophic wind. Figures 7b and 8b show that the ageostrophic winds on land were weaker because the total wind speed and its gradient were weaker there than that at sea. The distribution and intensity of the BLJ over the South China Sea were very different during the two heavy rainfall events. In case 1, most region of the third quadrant were located in the BLJ core. While in case 2, the range of the BLJ was smaller, and the third quadrant was mostly located to the southeast of the BLJ axis. The distribution of the IA ageostrophic wind component can be derived from Equations 5 and 6. Taking 1200 LST on May 22, 2013, as an example, Figure 11 shows the horizontal distribution of streamlines and total wind velocity. For point A, the curvature of the streamlines $K < 0$, and the variation of the total wind speed along with the streamlines $\partial V/\partial s < 0$, so the tangential ageostrophic wind component satisfied $V_{sa2} > 0$, and the normal component satisfied $V_{na2} < 0$. The result was that the ageostrophic wind component of IA term at this point was westerly. And for point B, $K \sim 0$ and $\partial V/\partial s < 0$, then we got $V_{sa2} \sim 0$ and $V_{na2} < 0$, so the ageostrophic wind component here was northwesterly. The results were consistent with Figure 7b. The same method can be used to verify the distribution of this ageostrophic wind component at other times and in case 2, which demonstrates that a difference in the distribution of BLJ can cause a difference in the ageostrophic wind component of the IA term.

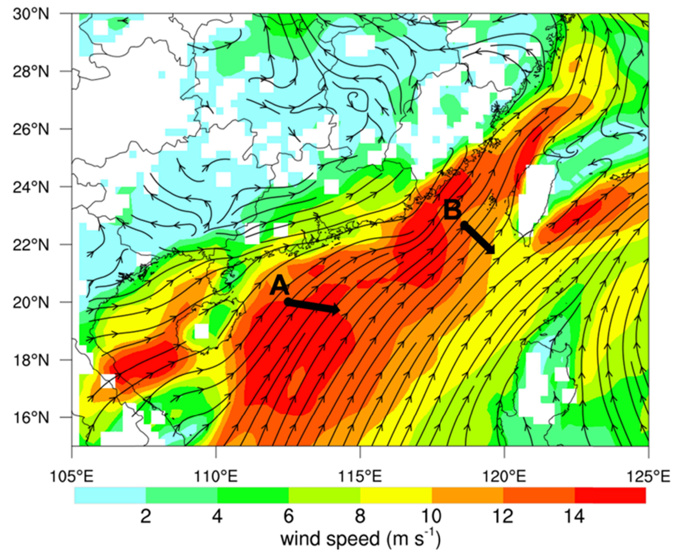

Figure 11. Horizontal distribution of streamlines of total winds (black streamlines) and total wind velocity (shading) at 925 hPa at 1200 LST 22 May 2013. The black dots are the locations of points A and B, and the black arrows are the ageostrophic wind components of the two points.

5.3 The Mechanisms of BE Term

In Figures 7c and 8c, the ageostrophic winds contributed by BE term were generally weak and only had a larger component in regions with large temperature gradients, such as the third quadrant in Figure 7c. Equation 4 shows that the ageostrophic wind component of BE term is mainly related to the temperature gradient and vertical velocity on the isobaric surface. Coastal South China is close to the tropics, and the temperature is generally high in May and June, so the temperature gradient is small, and the atmospheric baroclinic property is not notable, so the contribution of this term is limited. While the temperature gradient at sea in case 1 was larger than in case 2, and the temperature difference between sea and land was also larger in case 1 (Figures 9f and 10f), so the ageostrophic wind component of this term was also relatively stronger.

5.4 The Mechanisms of BLF Term

Figures 7d and 8d show that the BLF term was more notable than the other three terms on land, mainly due to land surface friction, and boundary layer turbulence friction. In addition, the term was also large in the BLJ region at sea, which could be explained by the fourth term on the right side in Equation 4. The magnitude of this term is proportional to the magnitude of the friction force, and the magnitude of the friction force is proportional to the total wind speed.

Therefore, the stronger the total wind speed is, the stronger the ageostrophic wind component contributed by the BLF term is, even on the oceanic surface. The BLJ is also subjected to strong friction, and the friction is stronger at sea in case 1 with a stronger and wider BLJ than in case 2. It's well known that the effect of friction is an ageostrophic deflection of the winds towards lower pressure, so the component of BLF term was almost easterly. The direction of the ageostrophic wind component of the BLF term can also be explained by Equation 4. Its direction is perpendicular to the friction and points to its right in the northern hemisphere. Considering that the direction of friction is opposite of the total wind velocity, the ageostrophic wind component is perpendicular to the total wind velocity pointing to its left in the northern hemisphere. In these two cases, the total wind speed was almost southerly and southeasterly on land (Figure 3), so the ageostrophic wind component was easterly and northeasterly.

6 Summary and Discussion

In this paper, two typical cases were selected from the WSHR events in the coastal region of South China influenced by the southwesterly BLJs. Both cases have strong convergence of ageostrophic winds at 925 hPa, which were the confrontational confluence type and asymptotic confluence type, respectively. The convergence can not only represent uplift conditions but also induce strong moisture convergence. This paper used the ERA5 reanalysis data to diagnose the contributions of the ageostrophic wind and to investigate the mechanisms that cause the convergence of ageostrophic winds. The main conclusions are as follows:

(1) The diagnostic equation of ageostrophic wind derived from the original horizontal momentum equation shows that the factors affecting the ageostrophic wind mainly include the local tendency of total wind speed, inertial advection, baroclinic effect, and boundary layer friction. The diagnostic analysis of typical cases shows that the main factors that contribute to the ageostrophic winds in the WSHR in South China were the local tendency of total wind speed and boundary layer friction. The inertial advection can also contribute to the ageostrophic wind component, while the contribution of baroclinic effects was not notable.

(2) The convergence of ageostrophic winds on the north and south sides of the rainfall area was caused by the difference between sea and land. On land, the BLF term dominates, contributing easterly and northeasterly ageostrophic winds. The diurnal variation of the LT component was obvious, but its wind speed was weaker, contributing little to the diurnal

variation of total ageostrophic wind. In contrast, at sea, the contribution of the LT term was more important, leading to a more distinct diurnal variation of ageostrophic wind direction and contributing a southerly ageostrophic wind. Therefore, there was a phase difference in the diurnal variation between the sea and land, causing convergence of ageostrophic winds on the coast and promoting the generation of WSHR.

(3) The BLJ in the South China Sea has an important impact on the ageostrophic winds and their confluence mode. Due to the strong total wind speed in the BLJ area, friction can contribute to strong ageostrophic winds. The areas with strong wind speed gradients in the BLJ area will contribute strong ageostrophic winds by the effect of inertial advection. In addition, if the diurnal variation of the BLJs is significant, strong ageostrophic winds will also be contributed by the local tendency of wind speed. Since the BLJ in case 1 was stronger and more extensive than in case 2, and its diurnal variation was also more significant, southwesterly ageostrophic wind component existed in the south of the rainfall area, producing a confrontational confluence pattern. And there was only an asymptotic confluence pattern in case 2.

(4) The land-sea thermal contrast can also influence the ageostrophic winds and their confluence mode. The land-sea thermal difference can affect the diurnal change of BLJs through the Holton mechanism, then affect the ageostrophic winds through the local tendency of the total wind. In case 2, the land-sea thermal difference was smaller at noon, so the v-component of the BLJ was stronger afternoon, making the behavior of the LT term in case 2 different from case 1. In addition, the greater thermal difference between land and sea also contributed stronger ageostrophic winds through the baroclinic effect, which is conducive to generating the confrontational confluence pattern in case 1.

In this paper, the diagnostic equation was used to decompose the ageostrophic wind into four terms, and the mechanisms of these terms were specifically investigated to explore the factors contributing to the ageostrophic winds and convergence in coastal WSHR in South China. These results show that the intensity and extent of BLJs and their diurnal variation can influence the ageostrophic winds and the strength and extent of convergence on the coast of South China. Land-sea thermal difference can also affect the ageostrophic winds. The important effects of southwest BLJs and land-sea thermal forcing were further verified, providing a better understanding of the WSHR process.

The present study is based on the reanalysis data and the selected two cases. In the future, more WSHR cases in the coastal area in South China will be studied to examine the effect of BLJs and land-sea thermal forcing in other atmospheric conditions, and their combined effect with other factors, such as terrain, should also be considered. We took the friction effect as the residual term of the diagnostic equation in this paper, so high-resolution numerical simulations are needed to verify its rationality and to investigate the detailed characteristics of different scales.

Acknowledgments

The authors are grateful to CMA for providing the merged precipitation data, and to ECMWF for providing the ERA5 reanalysis data. This work is supported by the National Natural Science Foundation of China (Grant 42075010).

Open Research

The precipitation data are obtained from CMDC (https://data.cma.cn/en), and users need to register first. Due to the current internal adjustment of the website, the data download has been temporarily suspended. After the service of the website is restored, the data used in this paper can be found by entering the keyword “CMORPH” in the search box. Before that, we recommend readers download other similar data, such as GPM IMERG Final Precipitation Product (https://doi.org/10.5067/GPM/IMERG/3B-HH/06), to carry out relevant research. The ERA-5 reanalysis data are available online (https://cds.climate.copernicus.eu/cdsapp#!/dataset/reanalysis-era5-pressure-levels?tab=form).

References

Barnes, S. L. (1964). A technique for maximizing details in numerical weather map analysis. *Journal of Applied Meteorology, 3*(4), 396–409. https://doi.org/10.1175/1520-0450(1964)003<0396:ATFMDI>2.0.CO;2

Barnes, S. L., & Colman, B. R. (1993). Quasigeostrophic diagnosis of cyclogenesis associated with a cutoff extratropical cyclone-The Christmas 1987 storm. *Monthly Weather Review, 121*(6), 1613-1634. https://doi.org/10.1175/1520-0493(1993)121<1613:QDOCAW>2.0.CO;2

Barnes, S. L., & Colman, B. R. (1994). Diagnosing an operational numerical model using Q-vector and potential vorticity concepts. *Weather and Forecasting, 9*(1), 85-102. https://doi.org/10.1175/1520-0434(1994)009<0085:DAONMU>2.0.CO;2

Blackadar, A. K. (1957). Boundary layer wind maxima and their significance for the growth of nocturnal inversions. *Bulletin of the American Meteorological Society, 38*(5), 283–290. https://doi.org/10.1175/1520-0477-38.5.283

Chen, G. T.-J., & Yu, C. C. (1988). Study of low-level jet and extremely heavy rainfall over northern Taiwan in the Mei-Yu season. *Monthly Weather Review, 116*(4), 884–891. https://doi.org/10.1175/1520-0493(1988)116,0884:SOLLJA.2.0.CO;2

Chen, G. T.-J., Wang, C.-C., & Lin, D. T.-W. (2005). Characteristics of low-level jets over northern Taiwan in Meiyu Season and their relationship to heavy rain events. *Monthly Weather Review, 133*(1), 20–43. https://doi.org/10.1175/MWR-2813.1

Chen, G.-X., Sha, W., & Iwasaki, T. (2009). Diurnal variation of precipitation over southeastern China: Spatial distribution and its seasonality. *Journal of Geophysical Research, 114*, D13103. https://doi.org/10.1029/2008JD011103

Chen, G.-X., Sha, W., Iwasaki, T., & Wen, Z. (2017). Diurnal cycle of a heavy rainfall corridor over East Asia. *Monthly Weather Review, 145*(8), 3365–3389. https://doi.org/10.1175/MWR-D-16-0423.1

Chen, X.-C., Zhao, K., & Xue, M. (2014). Spatial and temporal characteristics of warm season convection over Pearl River Delta region, China, based on 3 years of operational radar data. *Journal of Geophysical Research: Atmospheres, 119*(22), 12,447–12,465. https://doi.org/10.1002/2014JD021965

Chen, X.-C., Zhao, K., Xue, M., Zhou, B.-W., Huang, X.-X., & Xu, W.-X. (2015). Radar-observed diurnal cycle and propagation of convection over the Pearl River Delta during Mei-Yu season. *Journal of Geophysical Research: Atmospheres, 120*(24), 12557–12575. https://doi.org/10.1002/2015JD023872

Chen, X.-C., Zhang, F. Q., & Zhao, K. (2017). Influence of monsoonal wind speed and moisture content on intensity and diurnal variations of the Mei-Yu season coastal rainfall over south China. *Journal of the Atmospheric Sciences, 74*(9), 2835–2856. https://doi.org/10.1175/JAS-D-17-0081.1

Chen, X.-C., Zhang, F. Q., & Ruppert, J. H. (2019). Modulations of the diurnal cycle of coastal rainfall over south China caused by the boreal summer intraseasonal oscillation. *Journal of Climate, 32*(7), 2089–2108. https://doi.org/10.1175/JCLI-D-18-0786.1

Ding, Y. H. (1994). Monsoons over China. Dordrecht: Kluwer Academic Publishers.

Doswell, C. A., III, Brooks, H. E., & Maddox, R. A. (1996). Flash flood forecasting: An ingredients-based methodology. *Weather and Forecasting, 11*(4), 560-580. https://doi.org/10.1175/1520-0434(1996)011<0560:FFFAIB>2.0.CO;2.

Du, Y., & Chen, G.-X. (2018). Heavy rainfall associated with double low-level jets over southern China. Part I: Ensemble-based analysis. *Monthly Weather Review, 146(*11), 3827–3844. https://doi.org/10.1175/MWR-D-18-0101.1

Du, Y., & Chen, G.-X. (2019a). Heavy rainfall associated with double low- level jets over southern China. Part II: Convection initiation. *Monthly Weather Review, 147*(2), 543–565. https://doi.org/10.1175/MWR-D-18-0102.1

Du, Y., & Chen, G.-X. (2019b). Climatology of low-level jets and their impact on rainfall over southern China during early-summer rainy season. *Journal of Climate, 32*(24), 8813–8833. https://doi.org/10.1175/JCLI-D-19-0306.1

Du, Y., Chen, G.-X., Han, B., Mai, C.-Y., Bai, L.-Q., & Li, M.-H. (2020a). Convection initiation and growth at the coast of south China. Part I: effect of the marine boundary layer jet. *Monthly Weather Review, 148*(9): 3847–3869. https://doi.org/10.1175/MWR-D-20-0089.1

Du, Y., Chen, G.-X., Han, B., Bai, L.-Q., & Li, M.-H. (2020b). Convection Initiation and Growth at the Coast of South China. Part II: Effects of the Terrain, Coastline, and Cold

Pools. *Monthly Weather Review, 148*(9): 3871–3892. https://doi.org/10.1175/MWR-D-20-0090.1

Du, Y., & Rotunno, R. (2014). A simple analytical model of the nocturnal low-level jet over the Great Plains of the United States. *Journal of the Atmospheric Sciences, 71*(10), 3674–3683. https://doi.org/10.1175/JAS-D-14-0060.1

Du, Y., & Rotunno, R. (2018). Diurnal cycle of rainfall and winds near the south coast of China. *Journal of Atmospheric Sciences, 75*(6), 2065–2082. https://doi.org/10.1175/JAS-D-17-0397.1

Du, Y., Rotunno, R., & Zhang, Q.-H. (2015). Analysis of WRF-simulated diurnal boundary layer winds in eastern China using a simple 1D model. *Journal of the Atmospheric Sciences, 72*(2): 714–727. https://doi.org/10.1175/JAS-D-14-0186.1

Du, Y., Zhang, Q.-H., Chen, Y.-L., Zhao, Y.-Y., &Wang, X. (2014). Numerical simulations of spatial distributions and diurnal variations of low-level jets in China during early summer. *Journal of Climate, 27*(15), 5747–5767, https://doi.org/10.1175/JCLI-D-13-00571.1

Fu, P., Zhu, K., Zhao, K., Zhou, B., & Xue, M. (2019). Role of the nocturnal low-level jet in the formation of the morning precipitation peak over the Dabie mountains. *Advances in Atmospheric Sciences, 36*(1), 15–28. https://doi.org/10.1007/s00376-018-8095-5

Holton, J. R. (1967). The diurnal boundary layer wind oscillation above sloping terrain. *Tellus, 19*(2), 200–205, https://doi.org/ 10.1111/j.2153-3490.1967.tb01473.x

Holton, J. R.(2004). *An introduction to dynamic meteorology*. Academic Press. 88:139–181.

Huang, L., & Luo, Y. (2017). Evaluation of quantitative precipitation forecasts by TIGGE ensembles for south China during the pre-summer rainy season. *Journal of Geophysical Research: Atmospheres, 122*(16), 8494–8516. https://doi.org/doi:10.1002/2017JD026512

Huang, S. S. (1986). *Heavy Rainfall over Southern China in the Pre-Summer Rainy Season* (in Chinese). Guangdong Science and Technology Press, 244 pp.

Huang, X., Zhang, C., Fei, J., Cheng, X., Ding, J., & Liu, H. (2022). Uplift mechanism of coastal extremely persistent heavy rainfall (EPHR): The key role of low-level jets and ageostrophic winds in the boundary layer. *Geophysical Research Letters, 49*, e2021GL096029. https://doi.org/10.1029/2021GL096029

Huang, Y., Liu, Y., Liu, Y., Li, H., & Knievel, J. C. (2019). Mechanisms for a record-breaking rainfall in the coastal metropolitan city of Guangzhou, China: Observation analysis and nested very large eddy simulation with the WRF model. *Journal of Geophysical Research: Atmospheres, 124*, 1370–1391. https://doi.org/10.1029/2018JD029668

Koch, S. E., DesJardins, M., & Kocin, P. J. (1983). An interactive Barnes objective map analysis scheme for use with satellite and conventional data. *Journal of Climate and Applied Meteorology, 22*(9), 1487– 1503. https://doi.org/10.1175/1520-0450(1983)022<1487:AIBOMA>2.0.CO;2

Li, J., Li, N., & Yu, R. (2019). Regional differences in hourly precipitation characteristics along the western coast of South China. *Journal of Applied Meteorology and Climatology, 58*(12), 2717–2732. https://doi.org/10.1175/JAMC-D-19-0150.1

Li, X., & Du, Y. (2021). Statistical Relationships between Two Types of Heavy Rainfall and Low-Level Jets in South China, *Journal of Climate, 34*(21), 8549–8566. https://doi.org/10.1175/JCLI-D-21-0121.1

Lin, L. X., Feng, Y. R., & Huang, Z. (2006). T*echnical Guidance on Weather Forecasting in Guangdong Province* (in Chinese). Beijing: China Meteorological Press.

Liu, R. X., Sun, J. H., & Chen, B. F. (2019). Selection and classification of warm-sector heavy rainfall events over South China. Chinese Journal of Atmospheric Sciences, 43(1), 119−130, https://doi.org/10.3878/j.issn.1006-9895.1803.17245. (in Chinese)

Luo, Y., Wang, H., Zhang, R., Qian, W., & Luo, Z. (2013). Comparison of rainfall characteristics and convective properties of monsoon precipitation systems over South China and the Yangtze and Huai River Basin. *Journal of Climate, 26*(1), 110–132. https://doi.org/10.1175/JCLI-D-12-00100.1

Luo, Y., Zhang, R., Wan, Q., Wang, B., Wong, W. K., & Hu, Z., et al. (2017). The Southern China Monsoon Rainfall Experiment (SCMREX). *Bulletin of the American Meteorological Society, 98*(5), 999–1013. https://doi.org/10.1175/BAMS-D-15-00235.1

Luo, Y. H., & Du, Y. (2022). The roles of low-level jets in “21·7” Henan extremely persistent heavy rainfall event. Advances in Atmospheric Sciences. https://doi.org/10.1007/s00376-022-2026-1.

Shapiro, A., Fedorovich, E., & Rahimi, S. (2016). A unified theory for the Great Plains nocturnal low-level jet. *Journal of the Atmospheric Sciences, 73*(8), 3037–3057. https://doi.org/10.1175/JAS-D-15-0307.1

Shen, Y., Zhao, P., Pan, Y., & Yu, J. (2014). A high spatiotemporal gauge-satellite merged precipitation analysis over China. *Journal of Geophysical Research: Atmospheres, 119*(6), 3063–3075. https://doi.org/10.1002/2013JD020686

Slater, T. P., Schultz, D. M., & Vaughan, G. (2015). Acceleration of near-surface strong winds in a dry, idealised extratropical cyclone. *Quarterly Journal of the Royal Meteorological Society, 141*, 1004–1016, https://doi.org/10.1002/qj.2417

Sun, J., Zhang, Y., Liu, R., Fu, S., & Tian, F. (2019). A review of research on warm-sector heavy rainfall in China. *Advances in Atmospheric Sciences, 36*(12), 1299–1307, https://doi.org/10.1007/s00376-019-9021-1

Wei, P., Xu, X., & Xue, M. et al. (2022). On key dynamical processes supporting the 21.7 Zhengzhou record-breaking hourly rainfall in China. Advances in Atmospheric Sciences, https://doi.org/10.1007/s00376-022-2061-y.

Wu, M., Luo, Y., Chen, F., & Wong, W. K. (2019). Observed link of extreme hourly precipitation changes to urbanization over coastal South China. *Journal of Applied Meteorology and Climatology, 58*(8), 1799–1819. https://doi.org/10.1175/JAMC-D-18-0284.1

Wu, N., Ding, X., Wen, Z., Chen, G., Meng, Z., Lin, L., & Min, J. (2020b). Contrasting frontal and warm-sector heavy rainfalls over south China during the early-summer rainy season. Atmospheric Research, 235(10), 4693. https://doi.org/10.1016/j.atmosres.2019.104693

Wu, N. G., Zhuang, X. R., Min, J. Z., & Meng, Z. Y. (2020a). Practical and intrinsic predictability of a warm-sector torrential rainfall event in the south China monsoon region. *Journal of Geophysical Research: Atmospheres, 125*(4). https://doi.org/10.1029/2019JD031313

Xu, X., Xue, M., Wang, Y., & Huang, H. (2017). Mechanisms of secondary convection within a mei-yu frontal mesoscale convective system in eastern China. Journal of Geophysical Research: Atmospheres, 122, 47–64. https://doi.org/10.1002/2016JD026017

Xue, M., Luo, X., Zhu, K. F., Sun, Z. Q., & Fei, J. F. (2018). The Controlling Role of Boundary Layer Inertial Oscillations in Meiyu Frontal Precipitation and Its Diurnal Cycles Over China. Journal of Geophysical Research: Atmospheres, 123(10), 5090–5115. https://doi.org/10.1029/2018jd028368

Yuan, W., Yu, R., Chen, H., Li, J., & Zhang, M. (2010). Subseasonal Characteristics of Diurnal Variation in Summer Monsoon Rainfall over Central Eastern China. *Journal of Climate 23*(24), 6684-6695. https://doi.org/10.1175/2010JCLI3805.1

Zhang, C., Huang, X., Fei, J., Luo, X., & Zhou, Y. (2021). Spatiotemporal characteristics and associated synoptic patterns of extremely persistent heavy rainfall in southern China. *Journal of Geophysical Research: Atmosphere, 126*(1), https://doi.org/10.1029/2020JD033253

Zhang, M., & Meng, Z. (2018). Impact of synoptic-scale factors on rainfall forecast in different stages of a persistent heavy rainfall event in South China. *Journal of Geophysical Research: Atmospheres, 123*(7), 3574–3593. https://doi.org/10.1002/2017JD028155

Zhang, M., & Meng, Z. (2019). Warm-sector heavy rainfall in southern China and its WRF simulation evaluation: A low-level-jet perspective. *Monthly Weather Review, 147*(12), 4461–4480. https://doi.org/10.1175/mwr-d-19-0110.1

Zhou, X., Luo, Y., & Guo, X. (2015). Application of a CMORPH-AWS merged hourly gridded precipitation product in analyzing characteristics of short-duration heavy rainfall over southern China. *Journal of Tropical Meteorology, 31*(3), 333–344. https://doi.org/10.16032/j.issn.1004-4965.2015.03.005. (in Chinese)